Completely packed O(n) loop models and their relation with exactly solved coloring models

Yougang Wang,[1] Wenan Guo,[2,3,*] and Henk W. J. Blöte[1]
[1]*Lorentz Institute, Leiden University, P.O. Box 9506, 2300 RA Leiden, The Netherlands*
[2]*Physics Department, Beijing Normal University, Beijing 100875, People's Republic of China*
[3]*State Key Laboratory of Theoretical Physics, Institute of Theoretical Physics, Chinese Academy of Sciences, Beijing 100190, People's Republic of China*
(Received 1 November 2014; published 16 March 2015)

We investigate the completely packed O(n) loop model on the square lattice, and its generalization to an Eulerian graph model, which follows by including cubic vertices which connect the four incoming loop segments. This model includes crossing bonds as well. Our study was inspired by existing exact solutions of the so-called coloring model due to Schultz and Perk [Phys. Rev. Lett. **46**, 629 (1981)], which is shown to be equivalent with our generalized loop model. We explore the physical properties and the phase diagram of this model by means of transfer-matrix calculations and finite-size scaling. The exact results, which include seven one-dimensional branches in the parameter space of our generalized loop model, are compared to our numerical results. The results for the phase behavior also extend to parts of the parameter space beyond the exactly solved subspaces. One of the exactly solved branches describes the case of nonintersecting loops and was already known to correspond with the ordering transition of the Potts model. Another exactly solved branch, describing a model with nonintersecting loops and cubic vertices, corresponds with a first-order, Ising-like phase transition for $n > 2$. For $1 < n < 2$, this branch is interpreted in terms of a low-temperature O(n) phase with corner-cubic anisotropy. For $n > 2$ this branch is the locus of a first-order phase boundary between a phase with a hard-square, lattice-gas-like ordering and a phase dominated by cubic vertices. A mean-field argument explains the first-order nature of this transition.

DOI: 10.1103/PhysRevE.91.032123 PACS number(s): 05.50.+q, 64.60.Cn, 64.60.De, 75.10.Hk

I. INTRODUCTION

Several types of nonintersecting O(n) loop models can be obtained as a result of an exact transformation of certain O(n)-symmetric spin models [1–6]. Most of these models are two dimensional, but the transformation is also applicable in three dimensions [7]. It provides a generalization of the O(n) model to noninteger and even negative values of n. Whereas most existing work is restricted to nonintersecting loop models, the models can readily be generalized to include cubic vertices [8] and crossing bonds [9]. These cubic vertices connect to four incoming loop segments and arise naturally when the O(n) symmetry of the original spin model is broken by interactions of a cubic symmetry [10]. The crossing-bond vertices occur in the loop representation of nonplanar O(n)-symmetric spin models.

The presently investigated model is defined in terms of these three types of vertices on the square lattice. The three types, which are shown in Fig. 1 together with their vertex weights, specify a complete covering of the lattice edges. In comparison with a recent investigation [11] of crossover phenomena in a densely packed phase of the O(n) loop model, the present set of vertices is obtained by excluding those that do not cover all lattice edges. Due to the absence of empty edges, the physical interpretation in terms of an O(n) spin model is more remote. A formal mapping of the loop model on the spin model leads to a spin-spin interaction energy that can assume complex values when the relative weight of empty edges becomes sufficiently small. However, the mapping of the completely packed O(n) loop model on a dilute O($n-1$) loop model model (which was, as far as we know, first formulated by Blöte and Nienhuis; see Ref. [4]) brings it again closer to the realm of the spin models.

A configuration of the vertices of Fig. 1 forms a so-called Eulerian graph $\mathcal{G}$, in which only even numbers of loop segments are connected at each vertex. The present model may thus be called a completely packed Eulerian graph model. The partition sum of this model is

$$Z_{\mathrm{EG}} = \sum_{\mathcal{G}} z^{N_z} c^{N_c} x^{N_x} n^{N_n}. \tag{1}$$

The sum on $\mathcal{G}$ is on all compatible vertex coverings. The exponents N_z, N_c, and N_x are the numbers of vertices of types z, c, and x, respectively, and N_n is the number of components of the graph $\mathcal{G}$. A component is a subset of edges connected by a percolating path of bonds formed by the vertices of $\mathcal{G}$. Since Z_{EG} is a homogeneous function of the vertex weights, one may, without loss of generality, scale out one of the weights. We thus normalize the weight z of the O(n) vertex describing colliding loop segments to 1.

At this point it is appropriate to comment on our nomenclature. By "nonintersecting loops" we mean configurations consisting of the type-z vertices in Fig. 1. Since the word "intersecting" could be associated with the type-x vertices, as well as the type-c vertices in Fig. 1, we refer to type-x vertices as crossing bonds and to type-c vertices as cubic vertices. Thus, we may, alternatively, call this model a completely packed loop model with crossing bonds and cubic vertices, or just a generalized loop model. Furthermore, we note that the name "fully packed" is used for models where all vertices are visited, but not all edges are covered by loop segments [12,13].

The present work was inspired by a number of existing exact solutions, in particular of a "coloring model" by Schultz [14], later studied in more detail by Perk and Schultz [15] and others [16,17]; see also Fateev [18]. In the Perk-Schultz model, the edges of the square lattice receive one of several colors,

*Corresponding author: waguo@bnu.edu.cn

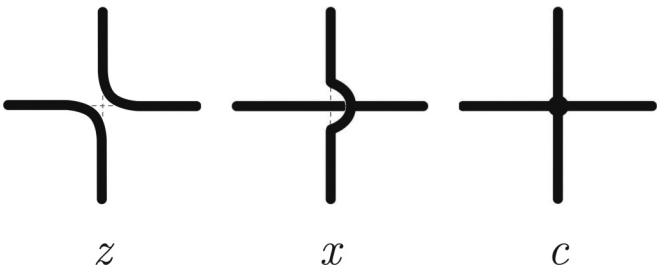

FIG. 1. The vertices of the completely packed O(n) loop model with crossing bonds and cubic vertices on the square lattice, together with their weights. Fourfold rotational symmetry of the model requires that the weights for the two possible orientations of the z-type vertex are the same.

in such a way that, for any given color, an even number of edges connects to each vertex. Exact solutions were found for several different branches of critical lines that are parametrized by the number of colors. Our purpose is to put them in the broader context of statistical physics by exploring the universal properties and phase behavior at and near their intersections with the phase diagram spanned by the parameters in Eq. (1).

The outline of this paper is as follows. In Sec. II we reformulate the Eulerian graph model in terms of the number of loops and describe the transformation connecting it to the coloring model. We review the exact results for the free energy, which apply to several one-dimensional "branches" parametrized by n in the parameter space of Eq. (1) and which are useful for the analysis of the conformal anomaly along these branches. This analysis is based on transfer-matrix calculations, for which some technical details are provided in Sec. III and the Appendix. Results for the free energy of the exactly solved branches are presented in Sec. IV and for some scaling dimensions in Sec. V. While the exploration of the complete (in fact three-dimensional) phase diagram of Eq. (1) is beyond the scope of the present paper, the embedding of some of the exactly solved branches in this diagram is investigated in Sec. VI. Our conclusions are presented and discussed in Sec. VII.

II. MAPPINGS AND EXISTING THEORY

A. Euler's theorem

Euler's theorem specifies that the number of components satisfies $N_n = N_s - N_b + N_l$, where N_s is the number of sites of the lattice, N_b is the number of bonds covered by $\mathcal{G}$, and N_l is the number of loops in $\mathcal{G}$. It means that every new bond decreases N_n by one, unless its end points were already connected. Application of this theorem to the present model requires some care because it merges the degrees of freedom of the cubic model with those of the O(n) model. Whereas the spins of the cubic model [8,19] are defined on the vertices of the square lattice, those of the square-lattice O(n) model [4,5] sit in the middle of the edges. Here we adopt the definition for the square-lattice O(n) loop model. Thus, the number N_s of sites in Euler's relation becomes twice the number N_v of vertices. Furthermore, in this formulation, a cubic vertex consists of *three* bonds: It connects one pair of sites along the x direction and one pair of sites along the y direction, and it also makes a connection between both pairs. Thus, for the present model, the number of bonds as required in Euler's formula is $N_b = 2N_z + 2N_x + 3N_c$, and Euler's theorem takes the form

$$N_n = N_s - 2N_z - 2N_x - 3N_c + N_l = N_l - N_c, \qquad (2)$$

where the last step uses $N_s = 2N_v$ and $N_v = N_z + N_x + N_c$ in the completely packed model. After substitution of Euler's theorem, the partition sum Eq. (1) is thus reformulated as

$$Z_{\mathrm{EG}} = Z_{\mathrm{loop}} = \sum_{\mathcal{G}} z^{N_z}(c/n)^{N_c} x^{N_x} n^{N_l}. \qquad (3)$$

The Boltzmann weights now only depend on the numbers of vertices of each type and on the number of loops. This formula exposes the nature of the partition sum as that of a generalized loop model: The number N_n of components is now absent, and the weight of a cubic vertex now appears as $c_n \equiv c/n$ instead of c. In this context it is noteworthy that the cubic weight c used in Ref. [11] is equal to $c_n = c/n$ when expressed in the parameters of the present work.

B. Relation with the coloring model

The Perk-Schultz coloring model is defined in Refs. [14,15] in terms of bond variables that can assume n different colors. The colors of the bonds connected to a given vertex are not independent. The number of bonds of a given color connected to a vertex is restricted to be even. Following Ref. [14], the vertex weights are denoted $R^{\lambda\mu}(\alpha\beta)$, where λ,μ denote the colors of the bonds in the $-x, +x$ directions and α,β apply to the $-y, +y$ directions, respectively. The color restrictions and symmetries are expressed by

$$R^{\lambda\mu}(\alpha\beta) = W^{\mathrm{d}}_{\alpha\lambda}\delta_{\alpha\beta}\delta_{\lambda\mu} + W^{\mathrm{r}}_{\alpha\beta}\delta_{\alpha\lambda}\delta_{\beta\mu} + W^{\mathrm{l}}_{\alpha\beta}\delta_{\alpha\mu}\delta_{\beta\lambda}, \qquad (4)$$

with

$$W^{\mathrm{r}}_{\alpha\beta} = W^{\mathrm{r}}(1-\delta_{\alpha\beta}), \quad W^{\mathrm{l}}_{\alpha\beta} = W^{\mathrm{l}}(1-\delta_{\alpha\beta}), \qquad (5)$$

and

$$W^{\mathrm{d}}_{\alpha\beta} = W^{\mathrm{d}}\delta_{\alpha\beta} + W^{0}(1-\delta_{\alpha\beta}). \qquad (6)$$

The weights thus satisfy the color permutation symmetry. We furthermore impose the symmetry condition

$$W^{\mathrm{l}} = W^{\mathrm{r}}, \qquad (7)$$

which leads to vertex weights that are invariant under rotations by $\pi/2$, thus allowing conformal symmetry of the coloring model in the scaling limit.

The model still contains, besides the number n of colors, three variable parameters W^0, W^{d}, and W^{r}. The partition sum of the coloring model is defined by

$$Z_{\mathrm{cm}} = \sum_{\mathcal{C}} \prod_{v} R^{\lambda_v\mu_v}(\alpha_v\beta_v), \qquad (8)$$

where the sum on $\mathcal{C}$ is over all colors of each bond and the product is over all vertices v. Each bond variable occurs twice in the product, once as a superscript and once as an argument of R.

In the absence of intersections between different colors, i.e., $W^{\mathrm{d}} = 0$, the coloring model is known to be equivalent with a Potts model and its Eulerian graph representation [20]. Here we provide the exact correspondence between the $W^{\mathrm{d}} \neq 0$

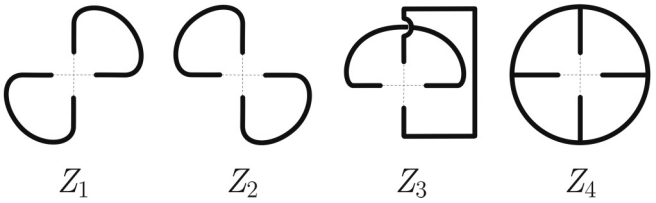

FIG. 2. The four different ways in which the incoming bonds at a vertex can be connected by the remaining configuration of the generalized loop model. The corresponding restricted partition sums are indicated under the figures.

coloring model [21] and the model of Eq. (3). This follows simply by the interpretation of the weight n of each component in Eq. (1) in terms of a summation on n different colors. Then the set of configurations of the loop model precisely matches that of the coloring model with weights according to Eqs. (4)–(6). The relation of the parameters W^{d}, W^0, and W^{r} with z, x, and c follows by matching the partition sums as expressed in the two types of vertex weights. After removing one vertex from $\mathcal{G}$, the connectivity of the incoming bonds, as determined by the surrounding loop model configuration, is denoted by an integer 1–4, specified in Fig. 2. The corresponding restricted partition sums of the generalized loop model are denoted as Z_1 to Z_4. They do not yet include the degeneracy factor n of the incomplete loops connected to the incoming bonds. In terms of these restricted sums and the local vertex weights of the coloring model, the partition sum is obtained by summation on the color combinations allowed by the diagrams in Fig. 2 as

$$\begin{aligned} Z_{\mathrm{cm}} = {} & [(n^2-n)W^{\mathrm{r}} + nW^{\mathrm{d}}](Z_1+Z_2) \\ & + [(n^2-n)W^0 + nW^{\mathrm{d}}]Z_3 + nW^{\mathrm{d}}Z_4. \end{aligned} \tag{9}$$

Using instead the local vertex weights of the generalized loop model, the partition sum follows, taking into account the weight n per component specified by Eq. (1), as

$$\begin{aligned} Z_{\mathrm{loop}} = {} & [(n^2+n)z + nx + nc](Z_1+Z_2) \\ & + n(2z+nx+c)Z_3 + n(2z+x+c)Z_4. \end{aligned} \tag{10}$$

The equivalence of both models requires that the prefactors of Z_1+Z_2, Z_3, and Z_4 are the same in both forms of the partition sum. These conditions lead to three equations, whose solution shows that the models are equivalent for

$$\left.\begin{aligned} W^0 &= x \\ W^{\mathrm{d}} &= 2z+x+c \\ W^{\mathrm{r}} &= z \end{aligned}\right\}. \tag{11}$$

In the representation of Eq. (1), the parameter n describing the number of colors is no longer restricted to positive integers.

C. The branches resulting from the solution of the coloring model

Several cases of the coloring model were studied analytically by Schultz [14]. That work provided analytic expressions for the partition sum per site. Included are results for a number of index-independent models, i.e., models satisfying Eqs. (4)–(6), so that all colors are equivalent. As noted above, the present work also restricts the vertex weight to be invariant under rotations by $\pi/2$, as required by asymptotic conformal invariance [22]. This enables the numerical estimation of some universal quantities as outlined in Sec. III.

TABLE I. Intersection between the exactly solved subspaces of the coloring model and the parameter space of the generalized loop model. These intersections form seven branches, defined in the first column, for which we also include the vertex weights. The entries under "Case" show the labeling used by Schultz [14], with the characters "a" and "b" appended in order to separate the Schultz cases into branches with single-valued vertex weights.

		Vertex weights		
Branch	Case	z	x	c
1	IIA1	1	0	0
2	IIA2a	1	0	$-1+\sqrt{n-1}$
3	IIA2b	1	0	$-1-\sqrt{n-1}$
4	IIB1a	1	$\frac{2-n}{4}$	0
5	IIB1b	1	$\frac{n-2}{4}$	$\frac{2-n}{2}$
6	IIB2a	0	1	0
7	IIB2b	0	1	-2

After application of these restrictions, the cases studied by Schultz reduce to seven one-dimensional subspaces in the parameter space of the loop model. These correspond, according to Eq. (11), with exactly solved "branches" of the generalized loop model of Eqs. (1) and (3). The vertex weights are shown in Table I as functions of n for these seven branches. These weights are normalized such that $z=1$, except for branches 6 and 7, where z vanishes, and we normalize as $x=1$ instead.

1. Branch 1

The exact solution of branch 1 by Schultz [14] is presented in terms of a quantity denoted there as f, which matches the per-site partition function, with the normalization $W^{\mathrm{d}}=1$ [15]. Branch 1 has nonzero weights only for colliding vertices of the z type, as shown in Fig. 1. It thus applies to a completely packed, nonintersecting loop model. For $n \geqslant 0$, this branch is exactly equivalent with the six-vertex model and with the $q=n^2$-state Potts model at its transition point [23]. Due to these equivalences, much is already known for branch 1. We recall some of these results for reasons of completeness as well as relevance for the interpretation of the phase diagram of Eq. (1).

Exact solutions of the aforementioned equivalent models were already given by Lieb [24] and Baxter [25], respectively. After taking into account the different normalizations of the vertices, and the fact that the number of Potts sites is one half of the number of vertices, the Schultz result for the free energy per vertex in the range $n > 2$ has been shown [26] to agree with the results of Lieb and Baxter in the corresponding parameter range. The Schultz result does not apply for $n \leqslant 2$, but there various other results for the free energy [24–28] are available. In the thermodynamic limit, the following results for the free energy per vertex apply:

$$f(n) = \frac{1}{2}\theta + \sum_{k=1}^{\infty} \frac{\exp(-k\theta)\,\tanh(k\theta)}{k}, \quad (n>2), \tag{12}$$

with θ defined by $\cosh\theta = n/2$;

$$f(2) = 2\ln\frac{\Gamma(1/4)}{2\,\Gamma(3/4)}, \tag{13}$$

$$f(n) = \frac{1}{2}\int_{-\infty}^{\infty} dx\,\frac{\tanh\mu x\,\sinh(\pi-\mu)x}{x\sinh\pi x}, \quad (-2 < n < 2), \tag{14}$$

where the parameter μ is defined by $\mu \equiv \arccos(n/2)$;

$$f(-2) = 0\,, \tag{15}$$

$$f(n) = \frac{1}{2}\tilde{\theta} + \sum_{k=1}^{\infty}\frac{[-\exp(-\tilde{\theta})]^k\,\tanh(k\tilde{\theta})}{k}\,, \quad (n < -2), \tag{16}$$

where $\cosh\tilde{\theta} = -n/2$. The expression for $n < -2$ applies [26] to the thermodynamic limit of a system with a number of vertices equal to a multiple of 4.

The correlation functions are known to follow a power law as a function of distance in the critical range $-2 \leqslant n \leqslant 2$ and to decay exponentially for $|n| > 2$. The off-critical phase for large n is known [26] to display the same type of order as the square lattice gas with nearest-neighbor exclusion.

2. Branches 2 and 3

These branches contain both colliding (z type) and cubic vertices (c type), as shown in Fig. 1, with a weight that depends on n. Their nature differs from branch 1 in the fact that different loops may now have common edges and vertices and thus be forced into the same component, according to Eq. (1).

In order to avoid confusion with our notation, we denote the Schultz result for the per-site partition function as z_S, instead of f as used there, which we reserve for the free-energy density. After substitution of the parameters as determined by Eq. (11) and Table I into the result [14] for z_S of branches 2 and 3 and some simplification, the free-energy per vertex follows as

$$\begin{aligned} f &= \ln(W^d z_S) \\ &= \ln\left\{\frac{n-1}{|-1\pm\sqrt{n-1}|}\prod_{k=1}^{\infty}\left[\frac{1\mp(n-1)^{-2k-1/2}}{1\mp(n-1)^{-2k-3/2}}\right]^2\right\}, \end{aligned} \tag{17}$$

where the upper signs in $\pm$ and $\mp$ apply to branch 2 and the lower signs apply to branch 3. This result applies to the thermodynamic limit of systems with an even number of vertices. Its validity cannot extend into the range $n < 2$, since the infinite product vanishes there. For $n \to 2$, branch 2, the infinite product compensates the divergence of the prefactor. Since branch 2 intersects with branch 1 at $n = 2$, its free energy at $n = 2$ is given by Eq. (13). For branch 3, the infinite product assumes the value 2 in the limit $n \to 2$, so that the free energy vanishes in this limit.

3. Branches 4 and 5

For branch 4, the system contains, in addition to the z-type colliding vertices, also x-type crossing-bond vertices (see Fig. 1), but no cubic vertices. A problem arises with the free-energy density corresponding with subcase IIB1 of Ref. [14], since it displays many divergences as a function of n. Furthermore, footnote [64] of Ref. [15], which applies to this result in Ref. [14], allows for the possibility that this result has to be modified by an additional factor. In order to determine this factor, we focus on the quantity z_S as given by Schultz [14]. In the present parameter subspace, it reduces to

$$z_S(n) = \frac{2-n}{4}\,\frac{\Gamma^2\left(\frac{1}{4}\right)}{\Gamma^2\left(\frac{3}{4}\right)}\,\frac{\Gamma\left(\frac{1}{2}+\alpha\right)\Gamma(1-\alpha)}{\Gamma\left(\frac{1}{2}-\alpha\right)\Gamma(\alpha)}, \quad \alpha \equiv \frac{6-n}{4(2-n)}. \tag{18}$$

After two applications of Euler's reflection formula, one finds

$$z_S(n) = \frac{2-n}{4}\,\frac{\Gamma^2\left(\frac{1}{4}\right)}{\Gamma^2\left(\frac{3}{4}\right)}\,\frac{\Gamma^2\left(\alpha+\frac{1}{2}\right)}{\Gamma^2(\alpha)}\,\mathrm{ctg}(\alpha\pi). \tag{19}$$

An independent calculation of the exact free-energy density of branch 4 is due to Rietman [29]. That result was derived for the intersecting loop representation in Eq. (3), whose relation with the coloring model was not immediately obvious. The Rietman expression for the free energy is free of divergences for $n < 2$. Numerical evaluation shows that, although the Schultz and Rietman results are different, they differ only by a fractional number for some fractional values of n. We thus cast the Rietman result z_R for the per-site partition function in a similar form as Eq. (19). It is [29]

$$\begin{aligned} z_R(n) = {} & \frac{4\kappa}{1+\kappa u(1-u)} \\ & \times \frac{\Gamma\left(1+\frac{u}{2}\right)\Gamma\left(\frac{3}{2}-\frac{u}{2}\right)\Gamma\left(\frac{1}{2}+\frac{1}{2\kappa}+\frac{u}{2}\right)\Gamma\left(1+\frac{1}{2\kappa}-\frac{u}{2}\right)}{\Gamma\left(\frac{1}{2}+\frac{u}{2}\right)\Gamma\left(1-\frac{u}{2}\right)\Gamma\left(\frac{1}{2\kappa}+\frac{u}{2}\right)\Gamma\left(\frac{1}{2}+\frac{1}{2\kappa}-\frac{u}{2}\right)}, \end{aligned} \tag{20}$$

where $\kappa \equiv 1 - \frac{n}{2}$, and u describes the anisotropy of the model when the two z-type colliding vertices have different weights, say z_1 and z_2 as $u = z_1/(z_1+z_2)$; in our work, $u = \frac{1}{2}$. Substitution of κ and u in Eq. (20) leads to

$$\begin{aligned} z_R(n) &= 16\,\frac{2-n}{10-n}\,\frac{\Gamma^2\left(\frac{5}{4}\right)}{\Gamma^2\left(\frac{3}{4}\right)}\,\frac{\Gamma^2\left[\frac{3n-10}{4(n-2)}\right]}{\Gamma^2\left[\frac{n-6}{4(n-2)}\right]} \\ &= \frac{2-n}{10-n}\,\frac{\Gamma^2\left(\frac{1}{4}\right)}{\Gamma^2\left(\frac{3}{4}\right)}\,\frac{\Gamma^2(\alpha+\frac{1}{2})}{\Gamma^2(\alpha)}, \end{aligned} \tag{21}$$

where the last equality uses the definition (18) of α. A comparison of Eqs. (19) and (21) shows that

$$z_S(n) = \frac{10-n}{2-n}\,\mathrm{ctg}(\alpha\pi)\,z_R(n). \tag{22}$$

The factor $(10-n)/(2-n)$ is equal to the weight ratio W^d/W^0 in the coloring model. The normalization used by Rietman, namely $2z + x = W^d = 1$, thus agrees with the normalization $W^0 = 1$ mentioned in Ref. [15] for the branch-4 result for z_S given in Ref. [14]. The remaining factor $\mathrm{ctg}(\alpha\pi)$ thus identifies the periodic factor mentioned in footnote [64] of Ref. [15]; we thus ignore it, so that the partition functions according to Refs. [14,29] become identical. The free-energy

density of branch 4 follows, in our normalization $z = 1$, as

$$f(n) = \ln\left[\frac{10-n}{4} z_{\mathrm{R}}\right] = \ln\left[\frac{2-n}{4}\,\frac{\Gamma^2\left(\frac{1}{4}\right)}{\Gamma^2\left(\frac{3}{4}\right)}\,\frac{\Gamma^2\left(\alpha+\frac{1}{2}\right)}{\Gamma^2(\alpha)}\right]. \tag{23}$$

This expression is well behaved for $n < 2$, but in the range $2 < n < 6$ it does not exhibit the expected type of behavior, because the arguments of the Γ functions can diverge and become negative. The fact that branches 1 and 4 intersect at $n = 2$ allows a consistency check by taking the limit $n \to 2$ in Eq. (23). Since α diverges, we may safely apply Stirling's formula. It then follows that the ratio of the divergent Γ functions just cancels the prefactor $2 - n$, so that we indeed reproduce Eq. (13).

The vertex weights for branch 5 differ from branch 4 in the additional presence of c-type cubic vertices. The Schultz result [14] for branch 5 specifies the same expression for the partition function as for branch 4. Later we compare our numerical results for branches 4 and 5 with Eq. (23) for several values of n.

4. Branches 6 and 7

The vertex weights of branches 6 and 7, given in Table I, do not depend on n, but the partition sum still contains the loop weight explicitly, and indeed it appears in the exact per-site partition sum z_{S} as given by Schultz [14]. This result leads to the free-energy density

$$f(n) = \ln[z_{\mathrm{S}}] = \ln\left\{\frac{\Gamma\left(\frac{1}{nb}\right)\Gamma\left[\frac{1+(n-2)b}{nb}\right]}{\Gamma\left(\frac{1-b}{nb}\right)\Gamma\left[\frac{1+(n-1)b}{nb}\right]}\right\}, \tag{24}$$

where

$$b = \frac{W^{\mathrm{r}}}{W^{\mathrm{d}}} = \frac{z}{2z+x+c} = 0.$$

Since we impose rotational symmetry over $\pi/2$ on the vertex weights by Eq. (7), and moreover $W^{\mathrm{l}}W^{\mathrm{r}} = 0$ for branches 6 and 7, we arrive at the special point $b = W^{\mathrm{r}} = z = 0$. We thus take the limit $b \to 0$ in Eq. (24):

$$f(n) = \lim_{b\to 0}\left\{\ln\Gamma\left(\frac{1}{nb}\right) + \ln\Gamma\left[\frac{1+(n-2)b}{nb}\right] - \ln\Gamma\left(\frac{1-b}{nb}\right) - \ln\Gamma\left[\frac{1+(n-1)b}{nb}\right]\right\}. \tag{25}$$

Each of the arguments of the Γ functions diverges in the limit of $b = 0$. We apply Stirling's formula and neglect terms that vanish in this limit:

$$\begin{aligned} f(n) = \lim_{b\to 0}\Bigg(&\left\{\frac{2-nb}{2nb}\,[-\ln(nb)] - \frac{1}{nb} + \frac{1}{2}\ln(2\pi)\right\} \\ &+ \left(\frac{2+nb-4b}{2nb}\,\{\ln[1+(n-2)b] - \ln(nb)\} - \frac{1+(n-2)b}{nb} + \frac{1}{2}\ln(2\pi)\right) \\ &- \left\{\frac{2-nb-2b}{2nb}\,[\ln(1-b) - \ln(nb)] - \frac{1-b}{nb} + \frac{1}{2}\ln(2\pi)\right\} \\ &- \left(\frac{2+nb-2b}{2nb}\,\{\ln[1+(n-1)b] - \ln(nb)\} - \frac{1+(n-1)b}{nb} + \frac{1}{2}\ln(2\pi)\right)\Bigg). \end{aligned}$$

We first consider the divergent terms with $\ln(nb)$. The sum of their amplitudes is seen to cancel exactly:

$$\frac{2-nb}{2nb} + \frac{2+nb-4b}{2nb} - \frac{2-nb-2b}{2nb} - \frac{2+nb-2b}{2nb} = 0.$$

Similarly, the sums of the amplitudes of terms with $\frac{1}{nb}$ and $\frac{1}{2}\ln(2\pi)$ vanish. Therefore,

$$\begin{aligned} f(n) = \lim_{b\to 0}\Bigg\{&\frac{2+nb-4b}{2nb}\ln[1+(n-2)b] \\ &- \frac{2-nb-2b}{2nb}\ln(1-b) \\ &- \frac{2+nb-2b}{2nb}\ln[1+(n-1)b]\Bigg\}. \end{aligned}$$

The prefactors depend linearly on $1/b$, and the logarithms are proportional to b in lowest order. It is therefore sufficient to keep the divergent part of the prefactors and the terms with b in the logarithms:

$$f(n) = \lim_{b\to 0}\left\{\frac{1}{nb}\,[(n-2)b + b - (n-1)b]\right\} = 0. \tag{26}$$

Thus, according to the Schultz solution, the free-energy density of branches 6 and 7 vanishes in the thermodynamic limit $L \to \infty$.

D. Exact results for the scaling dimensions and conformal anomaly

1. Results for branch 1

Although branch 1 can be mapped onto the critical Potts model, the exact results for the temperature and magnetic scaling dimensions of the Potts model do not apply to the completely packed system of branch 1 and the associated dense O(n) phase. Results for the magnetic dimension and the conformal anomaly of the dense O(n) phase have been obtained [30] from exact analysis of the model on the honeycomb lattice. These results coincide with the Coulomb

gas results given below and with an exact analysis of the model on the square lattice [31,32].

The Coulomb gas method, which offers a way to calculate some scaling dimensions, was explained in some detail in Ref. [10]. It considers an observable local density $p(r)$ on position r, which depends on the microstate at position r and is conjugate to the field q. In a critical state, we expect that the two-point correlation behaves as $\langle p(0)p(r)\rangle \propto r^{-2X_q}$, where the exponent X_q is the scaling dimension of the density p. Via the relation with the Coulomb gas one may now associate $p(0)$ with a pair of charges, an electric charge e_0, and a magnetic one m_0. Similarly, we have a pair e_r,m_r representing $p(r)$. Then, the scaling dimension X_q is given by [10]

$$X_q = X(e,m) = -\frac{e_0 e_r}{2g} - \frac{m_0 m_r g}{2}. \tag{27}$$

The Coulomb gas coupling g may be obtained if some exact information about the universal properties is available. Its determination, as well as that of the electric and magnetic charges, is a technical problem that we leave aside. We copy their values from the literature and present only the result in terms of X_q when needed.

For the critical O(n) model, as well as for its analytic continuation into the low-temperature O(n) phase, it is well established how to apply the Coulomb gas method [10]. In particular, the low-temperature O(n) phase, which shares its universal properties with the completely packed O(n) loop model of branch 1, is important for the present research. The Coulomb gas results include the following scaling dimensions of the critical O(n) model and the low-temperature phase:

$$X_h = 1 - \frac{3g}{8} - \frac{1}{2g}, \quad X_t = \frac{4}{g} - 2, \tag{28}$$

where X_t is the leading temperature dimension of the O(n) model. The Coulomb gas coupling constant g is given by

$$g = 1 \pm \frac{1}{\pi} \arccos\frac{n}{2}, \tag{29}$$

where the + sign applies to the critical O(n) model and the − sign to the dense low-temperature phase corresponding with branch 1. Furthermore, the introduction of the x- and c-type vertices into the nonintersecting O(n) loop model can be analyzed using the Coulomb gas [10,33]. These perturbations are described by the cubic-crossover exponent

$$X_c(g) = 1 + \frac{3g}{2} - \frac{1}{2g}. \tag{30}$$

This perturbation is relevant in the dense phase, thus crossing bonds and cubic vertices are expected to lead to different universal behavior in the range $-2 < n < 2$.

Next we express the conformal anomaly c_a as a function of the coupling constant g. From the definition of the parameter y as a function of n in Ref. [34], one finds that it relates to g by $y = 2 - 2g$ in our notation. Then, using Eqs. (1) and (9) of Ref. [34], one obtains the conformal anomaly as

$$c_\mathrm{a}(g) = 13 - 6g - \frac{6}{g}. \tag{31}$$

2. *Results for the other branches*

As far as we are aware, no exact results are available for the universal parameters of branches 2 and 3 and equivalent models. However, as mentioned in the preceding section, the cubic perturbation, i.e., the vertex weight c, is expected to introduce new universal behavior for branches 2 and 3 with respect to branch 1. Numerical results [11] for the dense phase (not completely packed) of the model with z- and c-type vertices confirm this and show the existence of a phase with a small value of the magnetic dimension X_h, i.e., a phase in which magnetic correlations persist over long distances.

The same Coulomb gas result applies to the introduction of crossing bonds, which is, like the cubic perturbation, also described by the four-leg watermelon diagram, and one may thus expect new universal behavior for branch 4. A few results are available for a supersymmetric spin chain [9] related to branch 4, referred to as the Brauer model [35,36]. Numerical as well as analytical arguments support, for $n \leqslant 2$, the formula for the conformal anomaly

$$c_\mathrm{a}(n) = n - 1, \quad (n \leqslant 2), \tag{32}$$

and the magnetic dimension X_h is reported to be very small, suggesting anomalously slow decay of magnetic correlations, at least for $n = 1$. This behavior was confirmed, although with limited accuracy, for a densely packed O(n) model with crossing bonds, which is believed to display similar universal behavior as branch 4 [11]. This model was also studied by Jacobsen *et al.* [37], and recently, correlation functions were obtained by Nahum *et al.* [38] for $n < 2$, decaying as an inverse power of the logarithm of the distance. As far as universal behavior is concerned, these findings for the completely packed model apply as well in the dense O(n) phase, but not for the O(n) transition to the high-temperature phase, where the cubic perturbation is irrelevant for $|n| < 2$. The latter point was numerically confirmed for the $n = 0$ [39] case, which describes intersecting trails.

III. TRANSFER-MATRIX METHOD

We use the transfer-matrix method to calculate the partition sum Z of a square lattice model, wrapped on the surface of a cylinder with a circumference of L lattice units. The cylinder may be infinitely long but its circumference L is finite. We postpone the transfer-matrix construction to the Appendix. Here we focus on the calculation of the free energy, the conformal anomaly and the scaling dimensions, which define the universality class. A finite-size analysis of the free energy does not only yield the conformal anomaly, but a comparison with the exact free energy, if available, provides a useful consistency check.

Free energy and correlation lengths

Using techniques described in the Appendix and in Ref. [40], we have computed a few of the leading eigenvalues of the transfer matrix $\mathbf{T}$ for some relevant parameter choices. We have restricted ourselves to eigenstates that are invariant under rotations about the axis of the cylinder and inversions. It follows from Eq. (A5) that, in general, the reduced free-energy density for $M \to \infty$ is determined by the largest eigenvalue

$\Lambda_0(L)$ as

$$f(L) = L^{-1} \ln \Lambda_0(L). \tag{33}$$

The transfer-matrix results for $f(L)$ can be used to estimate the conformal anomaly c_a using the relation [34,41]

$$f(L) \simeq f + \frac{\pi c_a}{6L^2}. \tag{34}$$

The subdominant eigenvalues $\Lambda_k(L)$ of $\mathbf{T}$ determine the correlation lengths ξ_k belonging to the kth correlation function. The gap with respect to the largest eigenvalue determines the corresponding correlation length along the cylinder as

$$\xi_k^{-1}(L) = \ln \frac{\Lambda_0}{|\Lambda_k|}, \tag{35}$$

where it is usual to associate the label $k = 1$ with the magnetic correlation length ξ_m and $k = 2$ with the energy-energy correlation length ξ_t. For the purpose of numerical analysis, it is convenient to define the corresponding scaled gaps $X_k(L)$ as

$$X_k(L) = \frac{L}{2\pi\xi_k(L)}. \tag{36}$$

In the presence of a temperature field t and an irrelevant field u, its scaling behavior is

$$X_k(t,u,L) \simeq X_k + aL^{y_t}t + bL^{y_u}u + \cdots, \tag{37}$$

where X_k is the scaling dimension of the observable whose correlation length is described by ξ_k [42]. This formula provides a basis to observe the phase behavior as a function of a parameter, such as a vertex weight, that contributes to t. If $y_t > 0$ and u is not too large, a set of curves displaying $X_k(L)$ versus that parameter for several values of the system size L will show intersections converging to the point where the relevant scaling field t vanishes, i.e., the point where a phase transition occurs. According to Eq. (37), the slopes of the $X_k(L)$ curves at the intersections increase with L if $y_t > 0$. In the data analysis, we make use of this criterion for the relevance of the scaling field t.

While the calculation of the temperaturelike scaling dimension $X_2 = X_t$ from Λ_2 is straightforward, that of the magnetic dimension X_h needs further comment. In the loop model, magnetic correlations between O(n) spins are represented by a single loop segment between the two sites. In completely packed models, it is not possible to add another loop segment into the system, and we use a method employed, e.g., in Ref. [11]. It analyzes the difference between the leading eigenvalues of systems with odd system size L containing such a segment and even systems without such a segment. Thus, one defines scaled gaps using the average of two consecutive even (or odd) systems as

$$X_h(\text{even } L) = \frac{L}{2\pi}\left\{\ln \Lambda_0(L) - \frac{1}{2}[\ln|\Lambda_1(L-1)| + \ln|\Lambda_1(L+1)|]\right\},$$

or

$$X_h(\text{odd } L) = \frac{L}{2\pi}\left\{\frac{1}{2}[\ln|\Lambda_0(L-1)| + \ln|\Lambda_0(L+1)|] - \ln \Lambda_1(L)\right\}, \tag{38}$$

where Λ_1 denotes the largest eigenvalue of odd systems in the transfer-matrix sector that includes an odd segment.

IV. NUMERICAL RESULTS FOR THE FREE ENERGY

This section presents the finite-size analysis of the transfer-matrix results for the free energy of the seven branches following from the Schultz solutions [14] and the mapping on Eqs. (1) and (3). The vertex weights for these seven branches are listed in Table I.

A. Branch 1

Some numerical results for branch 1 are already listed in Ref. [26], together with an analytic derivation of the free energy for $n < -2$. Here we summarize those results and provide additional data. The finite-size data for the free energy were extrapolated using Eq. (34), yielding estimates of $f(n)$, which are listed in Table II. For $n = -2$, the finite-size data for the free energy did not obey Eq. (34), but were, up to numerical precision, precisely proportional to $1/L$. Accordingly, we quote the results $f(-2) = 0$ and, for the conformal anomaly, $c_a = -\infty$. For most values of n, these free energies agree satisfactorily with the theoretical values given in Eqs. (12) to (16). Next, the free energies in Eq. (34) were fixed at their theoretical values, in order to obtain improved estimates of the conformal anomaly. These results are also listed in Table II and appear to agree well with the theoretical values, except for the ranges where $|n|$ slightly exceeds 2 and where poor finite-size convergence occurs.

B. Branches 2 and 3

The finite-size data for the free energy of branch 2 were fitted by Eq. (34). Fits with two iteration steps, as described, e.g., in Ref. [40], were employed, using various combinations of exponents that were left free or fixed at expected integer values. A comparison between the different fits, and between fits using even and odd system sizes, thus yielded error estimates. The best estimates of $f(n)$ are listed in Table III.

One observes that the bulk free energy for $n > 2$ is in agreement with the Schultz solution [14]. Since branches 1 and 2 intersect at $n = 2$, we took the $n = 2$ exact result for branch 1 in the second column of Table III. For $n = 1$, branches 2 and 3 are connected and the partition sum allows independent summation on the vertex states, which yields a factor 1 per vertex. This yields the exact results $f(1) = 0$ and $c_a = 0$, also shown in Table III. For $n = 2$, branch 3, the largest eigenvalue of the transfer matrix is 2 for all even system sizes; therefore, the bulk free energy and the conformal anomaly also vanish in this case.

While the bulk free energy is well resolved in most cases, complications arise for the part of branch 3 with small n. The free energy for a small system seems to converge well to a limiting value as

$$f(n) = \pm\sqrt{n-1} + \tfrac{1}{2}(n-1) \mp \tfrac{5}{3}(n-1)^{3/2} + \cdots, \tag{39}$$

where the upper signs apply to branch 2 and the lower sign to branch 3. This behavior agrees well with the numerical data for larger n in the case of branch 2, but not with those for branch 3. There appears to be an eigenvalue crossing for branch 3, which, for $n = 1.05$, occurs at $L = 10$, near the middle of

TABLE II. Fit results for the free-energy density and the conformal anomaly of the branch 1 model, compared with the theoretical values. Estimated numerical uncertainties in the last decimal place are given between parentheses. The entries "0 (−)" indicate that the raw numerical data agree, up to numerical precision, with a vanishing result.

n	f_{exact}	f_{extr}	$c_{a,\text{exact}}$	$c_{a,\text{extr}}$
–20	1.447 952 861 454	1.447 952 8(1)	0	0.000 000 (1)
–10	1.052 018 311 561	1.05202 (1)	0	0.001 (1)
–4.0	0.456 613 026 255	0.45 (5)	0	0 (50)
–3.0	0.252 039 567 005	0.26 (4)	0	20 (40)
–2.0	0	0.005 (2)	$-\infty$	$-\infty$ (−)
–1.8	0.207 751 892 795	0.2078 (3)	−29.653 937 4	−29.65 (2)
–0.2	0.557 322 110 937	0.557 322(1)	−2.626 037 87	−2.626 04 (1)
0.0	0.583 121 808 062	0.582 (1)	−2	−1.9998 (5)
0.2	0.607 404 530 379	0.607 404 53(1)	−1.471 954 92	−1.471 955 00 (5)
0.4	0.630 389 998 897	0.630 389 999(5)	−1.021 086 33	−1.021 086 4 (2)
0.6	0.652 252 410 906	0.652 252 411(3)	−0.632 395 53	−0.632 395 6 (2)
0.8	0.673 132 748 867	0.673 132 749(2)	−0.294 808 10	−0.294 808 2 (1)
1.0	0.693 147 180 560	0.693 147 180 56(1)	0	0 (−)
1.2	0.712 392 984 154	0.712 392 984(1)	0.258 345 80	0.258 345 9(1)
1.4	0.730 952 859 626	0.730 952 860(2)	0.484 999 81	0.485 000 0(1)
1.6	0.748 898 172 077	0.748 898 172(2)	0.683 414 06	0.683 414 0(1)
1.8	0.766 291 499 497	0.766 291 499(2)	0.855 601 57	0.855 610(2)
2.0	0.783 188 785 414	0.783 188 75(3)	1	1.002 (1)
2.5	0.823 597 622 499	0.823 597(1)	0	1.304 (?)
3.0	0.861 997 334 707	0.862 05(3)	0	1.6 (?)
4.0	0.934 112 909 108	0.9341 (1)	0	–0.1 (5)
6.0	1.059 762 003 273	1.059 76(1)	0	0.0000 (5)
8.0	1.163 519 822 868	1.163 519 5(3)	0	0.000 00 (3)
10	1.250 668 806 419	1.25066880 (5)	0	0.000 00(1)
15	1.420 503 142 656	1.420 503 142 7(2)	0	0.000 000(1)
20	1.547 785 693 447	1.547 785 693 4(1)	0	0.000 000 00(1)

the range of accessible system sizes. The eigenvalue crossings shift to smaller L for larger values of n. Thus, we believe that Eq. (39) does not apply to the bulk free energy of branch 3, not even for n close to 1. In addition to the level crossing, the free-energy data display oscillations with a period 4 in the system size for branch 3. For these reasons the free energies of branch 3 could not be accurately determined in the interval $1 < n < 2$.

The conformal anomaly for branch 2 was estimated by least-squares fits on the basis of Eq. (34), with the finite-size exponent fixed at -2. These fits do not show the type of fast convergence as that of branch 1. Especially for $n < 2$, we observe that strong crossover effects play a role, so that the errors are difficult to estimate. For $n > 2$, there exists a range of n where the numerical results seem to suggest, as indicated in the table, a conformal anomaly $c_{\text{a}} > 1$, but iterated fits display a diverging trend, which becomes progressively stronger with increasing n. Thus, the entries for c_{a} in Table III for $2 < n < 2.6$ may not be taken too seriously. For larger n, the data are no longer suggestive of convergence to a value of $c_{\text{a}} > 0$. Only for $n \gtrsim 20$ do we observe the exponential convergence of the free energy with L that is expected in a noncritical phase, corresponding with $c_{\text{a}} = 0$.

For branch 3, the finite-size data for f are, remarkably, behaving more like $f(L) = f(\infty) + a/L$, which does not suggest a finite conformal anomaly. For $n \gtrsim 5$, the absolute value of the effective exponent becomes significantly larger than 1 and tends to increase with L, in accordance with the expected crossover to exponential behavior, which is indeed seen for $L \gtrsim 25$. Convergence is poor in the crossover range around $n = 10$, and the extrapolated values of the free energy are relatively inaccurate in that range.

An investigation into how branches 2 and 3 are embedded in the c_n versus n phase diagram is reported in Sec. VI.

C. Branch 4

The branch-4 system contains crossing bonds instead of the cubic vertices considered in the preceding section. The largest eigenvalues of the transfer matrix were computed for a number of values of the loop weight n for system sizes up to $L = 16$. The extrapolated values of the free-energy density for $n \leqslant 2$ agree accurately with the exact expression given by Eq. (23), as shown in Table IV. That expression does, however, no longer agree with the numerical results listed for the range $n > 2$.

However, the free-energy data listed in Table IV accurately display a symmetry with respect to the point $n = 2$. It is thus straightforward to conjecture an exact expression for the free-energy density along branch 4 for all n, by replacing $n - 2$ with $|n - 2|$ in Eq. (23):

$$f(n) = \ln\left(\frac{|n-2|}{4}\right) + 2\ln\Gamma\left(\frac{1}{4}\right) - 2\ln\Gamma\left(\frac{3}{4}\right) - 2\ln\Gamma\left(\frac{1}{4} + \frac{1}{|n-2|}\right) + 2\ln\Gamma\left(\frac{3}{4} + \frac{1}{|n-2|}\right). \tag{40}$$

TABLE III. Numerical results for the free-energy density of the branch 2 and 3 models, compared with the theoretical values. Fit results for the conformal anomaly of branch 2 are also shown. Estimated numerical uncertainties in the last decimal places are given between parentheses. The entries "0 (−)" indicate that the raw numerical data agree, up to numerical precision, with a vanishing result.

	Branch 2			Branch 3	
n	f_{exact}	f_{extr}	$c_{a,\text{extr}}$	f_{exact}	f_{extr}
1.0	0	0 (−)	0 (−)	0	0.0 (−)
1.1		0.321 623(2)	0.00 (1)		0.113 (2)
1.2		0.435 512(5)	0.0 (1)		0.140 (2)
1.4		0.571 672(5)	0.3 (2)		0.158 (3)
1.6		0.660 925(1)	0.4 (2)		0.152 (5)
1.8		0.728 440 4(5)	0.85 (2)		0.126 (5)
1.9		0.757 079 9(2)	0.930 (2)		0.10 (1)
2.0	0.783 188 785 4	0.783 188 8(1)	1.002 (1)	0	0.0 (−)
2.2	0.829 461 794 7	0.829 461 8(2)	1.12 (1)	0.047 659 412 4	0.047 66(2)
2.4	0.869 666 581 0	0.869 666 5(5)	1.2 (1)	0.091 211 110 0	0.091 21(2)
2.6	0.905 296 142 0	0.905 296(1)		0.131 374 954 4	0.131 75(5)
2.8	0.937 343 816 2	0.937 344(2)		0.168 712 229 2	0.168 72(1)
3.0	0.966 505 681 1	0.966 506(2)		0.203 665 531 7	0.203 65(2)
3.2	0.993 289 405 5	0.993 290(3)		0.236 589 317 3	0.236 55(5)
3.4	1.018 077 210 8	1.018 078(2)		0.267 768 629 8	0.2677 (1)
3.6	1.041 164 429 3	1.041 165(2)		0.297 431 470 8	0.2972 (2)
3.8	1.062 784 230 9	1.062 785(2)		0.325 759 322 2	0.3254 (2)
4.0	1.083 124 091 3	1.083 125(1)		0.352 896 832 0	0.3525 (2)
5.0	1.170 171 212 8	1.170 166(1)		0.474 147 692 7	0.473 (1)
10.	1.436 020 923 3	1.4362 (3)		0.876 274 779 5	0.88 (1)
15.	1.594 492 588 8	1.5945 (3)		1.117 947 417 0	1.118 (3)
20.	1.709 737 605 6	1.7098 (3)	0.0 (5)	1.288 477 791 3	1.2885 (5)
25.	1.800 936 424 8	1.800 93(5)	0.01 (5)	1.419 532 589 5	1.419 54(5)
30.	1.876 647 802 1	1.876 65(2)	0.01 (2)	1.525 657 439 2	1.525 67(2)
50	2.094 338 030 3	2.094 337(1)	0.001 (2)	1.818 084 562 3	1.818 084(5)
100	2.401 469 246 9	2.401 692(1)	0.000 (1)	2.203 800 912 7	2.203 800(2)

Whereas the bulk free energy displays a clear symmetry with respect to the point $n = 2$, this is not the case for the finite-size results for the free energy. Accordingly, the estimated values of the conformal anomaly, also included in Table IV, do not obey the symmetry. These estimates of c_{a} were obtained by fits according to Eq. (34), with the bulk free energy fixed according to Eq. (40). Our confidence in this procedure is based on the degree of accuracy found above for the agreement between the extrapolated values of the free energy and Eq. (40).

In the range $n \leqslant 2$, the results for the conformal anomaly are suggestive of behavior according to Eq. (32). While the finite-size dependence of the estimates of c_{a} is quite small, their apparent convergence is very slow in this range. This makes it difficult to estimate the error margins, so that our new evidence supporting Eq. (32) may not be considered as very convincing. The fits for c_{a} in the range $n \geqslant 2$ are better behaved, and the numerical results in Table IV allow the conjecture

$$c_{\text{a}} = n/2 \quad (n \geqslant 2). \tag{41}$$

This type of behavior is already strongly suggested by first estimates of c_{a} as $6\pi^{-1}L^2[f(L) - f(\infty)]$. Such estimates in the range $3 \leqslant n \leqslant 8$ differ less than 10^{-2} from $n/2$ for $L = 16$. However, apparent convergence is slow, and we were unable to reduce the estimated uncertainty margins much below the 10^{-2} level by means of iterated fits.

D. Branch 5

The definition of branch 5 specifies that both crossing bonds and cubic vertices occur in addition to the original O(n)-type vertices. In the representation of the coloring model, the vertex weights of branch 5 according to Eq. (11) are equal to those for branch 4, except for a change of sign of the weight W^0 describing a color crossing. In an infinite system, such crossings occur in pairs, so that the free-energy density for branch 5 must be equal to that for branch 4. This may be expected to hold also for finite systems with an even system size, which is confirmed by our transfer-matrix results for the largest eigenvalue, at least for $n > -2$. A level crossing occurs at $n = -2$, and for $n < -2$ the largest eigenvalue of a system with a size L divisible by 4 has an eigenvector that is antisymmetric under translations. Such eigenvalues do not contribute to the free energy of a translationally invariant system. For systems with a size equal to an odd multiple of 2, the largest eigenvalues of branch 4 coincide with those of branch 5, also for $n < -2$.

Another point of interest is that, in the representation of the generalized loop model, the vector space of the transfer matrix for the branch-5 model is larger than that for branch 4, due to the larger number of connectivities in the presence of cubic vertices. This leads to additional eigenvalues and thus to additional scaling dimensions for branch 5.

TABLE IV. Fit results for the bulk free-energy density of branches 4 and 5, compared with the theoretical values $f_{\rm R}$ given by Rietman [29]. Estimated numerical uncertainties in the last decimal place are given between parentheses. Error margins quoted as "(−)" indicate that the raw finite-size data agree, with a numerical precision determined only by rounding errors, with the listed result. This table is organized such as to display the symmetry $f(2+x) = f(2-x)$ of the free energy. Results for the conformal anomaly, estimated from the finite-size dependence of the free-energy data, are also listed.

n	$f_{\rm R}$	$f_{\rm extr}$	$c_{a,\rm extr}$	n	$f_{\rm extr}$	$c_{a,\rm extr}$
2.0	0.783 188 785 414	0.783 190(2)	1.002 (2)	2.0	0.783 190(2)	1.002 (2)
1.6	0.788 072 581 927	0.788 072(2)	0.66 (1)	2.4	0.788 070(4)	1.32 (2)
1.2	0.801 609 709 369	0.801 610(2)	0.22 (1)	2.8	0.801 607(5)	1.40 (1)
1.0	ln(9/4)	ln(9/4) (−)	0 (−)	3.0	0.810 929(2)	1.50 (1)
0.8	0.821 583 452 525	0.821 58(1)	–0.22 (2)	3.2	0.821 583(1)	1.60 (1)
0.6	0.833 330 017 842	0.833 33(1)	–0.44 (3)	3.4	0.833 329(1)	1.70 (1)
0.4	0.845 964 458 726	0.845 96(1)	–0.65 (5)	3.6	0.845 964(1)	1.80 (1)
0.2	0.859 313 113 225	0.859 31(1)	–0.92 (8)	3.8	0.859 313(1)	1.90 (1)
0.0	0.873 230 390 267	0.873 23(1)	–1.1 (1)	4.0	0.873 230(1)	2.003 (5)
–0.2	0.887 594 745 620	0.887 60(1)	–1.3 (2)	4.2	0.887 594(1)	2.103 (5)
–0.4	0.902 304 904 172	0.902 30(1)	–1.6 (2)	4.4	0.902 304(1)	2.202 (5)
–0.6	0.917 276 530 696	0.917 27(1)	–1.8 (2)	4.6	0.917 276(1)	2.302 (5)
–0.8	0.932 439 389 367	0.932 43(2)	–2.0 (3)	4.8	0.932 439(1)	2.402 (5)
–1.0	0.947 734 962 298	0.947 73(1)	–2.2 (3)	5.0	0.947 735(1)	2.502 (5)
–1.2	0.963 114 471 587	0.963 11(1)	–2.5 (3)	5.2	0.963 114(1)	2.603 (5)
–1.6	0.993 969 362 786	0.993 97(1)	–2.9 (4)	5.6	0.993 969(1)	2.802 (5)
–2.0	1.024 753 260 684	1.0247 (1)	–3.4 (5)	6.0	1.024 752(1)	3.002 (5)
–2.5	1.062 873 680 798	1.0629 (1)	−4 (1)	6.5	1.062 87(1)	3.25 (1)
–3.0	1.100 390 077 368	1.1004 (2)	−5 (1)	7.0	1.100 38(1)	3.51 (1)
–4.0	1.173 116 860 698	1.1731 (5)	−6 (2)	8.0	1.173 11(2)	4.00 (2)
–6.0	1.308 199 777 002	1.308 (3)	−10 (2)	10.0	1.3082 (2)	5.0 (1)
–8.0	1.429 801 657 071	1.43 (3)		12.0	1.4298 (2)	6.0 (2)

After verification that the leading transfer-matrix eigenvalues for branches 4 and 5 coincide, there is no reason for a separate analysis of the free energy of branch 5 besides that of branch 4.

E. Branches 6 and 7

The transfer-matrix results for the free-energy density $f(n,L)$ of finite branch-6 systems are found to behave precisely as

$$f(n,L) = \frac{\ln(n)}{L}, \tag{42}$$

and those for branch 7 as

$$f(n,L) = \begin{cases} L^{-1}\ln(n) & (L \text{ even}), \\ L^{-1}\ln(n-2) & (L \text{ odd}). \end{cases} \tag{43}$$

The apparent simplicity of these results is due to the conservation of colors along lines of vertices, or the absence of z-type vertices for branches 6 and 7. This condition is imposed by the symmetry requirement Eq. (7). For branch 6, there are only x-type vertices, and every layer of vertices trivially contributes a weight n for a loop closing around the cylinder, thus explaining Eq. (42). The coloring-model parameters of branch 7 are $W^0 = 1$, $W^{\rm d} = -1$. The leading eigenvalue of the transfer matrix occurs in the sector in which the colors on the lines parallel to the axis of the cylinder are the same. Summation on the n colors of a newly added layer thus contributes $n - 1 + (-1)^L$, which yields n for even systems and $n-2$ for odd ones, in agreement with Eq. (43).

These results imply that the bulk free energy vanishes for branches 6 and 7. This agrees with the Schultz solution which, in the symmetric case described by Eq. (7), becomes trivial, as expressed by Eq. (26).

V. EVALUATION OF SCALING DIMENSIONS

In view of the trivial nature of branches 6 and 7 described in the preceding section, these do not require further analysis. This section focuses on the transfer-matrix results for the scaling dimensions of branches 1 to 5.

A. Branch 1

The extrapolated results for the temperature dimension X_t, and those for the magnetic dimension X_h are, together with the exact Coulomb gas predictions [10], listed in Table V for several values of the loop weight n. These results supplement earlier data for the temperature dimension listed in Ref. [26], and data for the dense (not completely packed) phase of the O(n) model [4], which is related by universality. For $n \geqslant 1$ the extrapolated transfer-matrix results for the leading temperaturelike dimension agree with the Coulomb gas result for X_t, but this is no longer the case for $n < 1$, where the extrapolations seem to converge to the exact value 4. The Coulomb gas values for X_t are omitted in most of the range $n < 1$, where they no longer match the numerical results. Calculations of the three leading eigenvalues whose eigenvectors satisfy the translational and inversion symmetries of the lattice indicate that the scaling dimension $X_t = 4$ still

TABLE V. Fit results for the temperature dimension X_t and the magnetic dimension X_h of the branch 1 model, compared with the theoretical values. Estimated numerical uncertainties in the last decimal place are given between parentheses. The entries "0 (−)" indicate that the raw numerical data for finite systems agree, up to numerical precision, with a vanishing result.

n	$X_{t,\mathrm{extr}}$	$X_{t,\mathrm{exact}}$	$X_{h,\mathrm{extr}}$	$X_{h,\mathrm{exact}}$
–2.0	0 (−)		0 (−)	$-\infty$
–1.8	4.1 (1)		–2.5360 (5)	−2.536 549 00 ···
–1.6	4.01 (1)		−1.517 82 (2)	−1.517 828 01 ···
–1.4	4.002 (2)		−1.067 97 (1)	−1.069 797 45 ···
–1.2	4.000 (1)		−0.804 642 (1)	−0.804 642 67 ···
–1.0	4.0000 (1)		−0.625 000 0 (1)	−0.625 000 00 ···
–0.8	4.0000 (1)		−0.493 355 2 (2)	−0.493 355 19 ···
–0.6	4.0000 (1)		−0.391 783 8 (1)	−0.391 783 79 ···
–0.4	4.000 00(1)		−0.310 501 5 (1)	−0.310 501 53 ···
–0.2	4.000 000(2)		−0.243 655 4 (1)	−0.243 655 36 ···
0.0	4.000 001(1)		−0.187 500 0 (1)	−0.187 500 00 ···
0.2	4.000 000(1)		−0.139 510 7 (1)	−0.139 510 71 ···
0.4	4.000 01(2)	5.0910···	−0.097 912 1 (1)	−0.097 912 08 ···
0.6	3.999 99(2)	4.7003···	−0.061 409 6 (1)	−0.061 409 63 ···
0.8	4.000 (1)	4.3392···	−0.029 026 9 (1)	−0.029 026 94 ···
1.0	4.000 (2)	4.0000···	0 (−)	0.000 000 00···
1.2	3.68 (2)	3.6751···	0.026 299 5(1)	0.026 299 58···
1.4	3.357 (2)	3.3561···	0.050 435 3(1)	0.050 435 40···
1.6	3.029 (2)	3.0304···	0.073 015(1)	0.073 013 74···
1.8	2.67 (1)	2.6705···	0.095 032(5)	0.095 021 01···
2.0	2.1 (1)	2.0000···	0.122 (1)	0.125 000 00···

exists for $n > 1$, as well as that predicted by the Coulomb gas theory in the range $n < 1$. This is illustrated in Fig. 3, which shows the two leading temperaturelike scaled gaps for system sizes $L = 8$, 10, 12, 14, and 16.

The data for X_h in Table V agree well with the Coulomb gas results, except near $|n| = 2$. Poor finite-size convergence occurs near $n = 2$, and for $n = -2$, the whole eigenvalue spectrum of finite systems collapses to $|\Lambda_i| = 2$, corresponding with $X_t = X_h = 0$. However, we expect a different result for these scaling dimensions when the order of the limits $n \to -2$ and $L \to \infty$ is reversed.

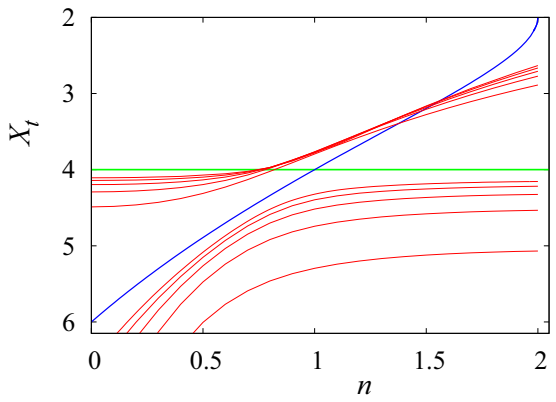

FIG. 3. (Color online) The two leading thermal scaled gaps of the branch-1 model versus loop weight n for even system sizes $L = 8$ to 16. The scaled gaps are shown as thin lines, smoothly connecting a series of data points. The scaled gaps increase with L in most of the range of n. Also shown are two thicker lines, of which one represents a constant scaling dimension $X = 4$ and the other the Coulomb gas result for X_t. Extrapolation of the finite-size data indicates that the leading gap (upper set of curves) converges to $X_t = 4$ for $n < 1$ and to the Coulomb gas result for X_t for $n > 1$. The second gap behaves similarly but with the intervals of n interchanged.

The data for $|n| \geqslant 10$ show a divergent behavior of the scaled gaps, in agreement with the expected absence of criticality for large $|n|$. Extrapolations for $|n| \gtrsim 2$ (not shown in Table V) are consistent with the presence of a marginally relevant operator at $|n| = 2$. The ranges $|n| > 2$ of branch 1 have earlier been identified [26] as lines of phase coexistence, separating two lattice-gas-like ordered phases. The associated vanishing scaling dimension corresponds with an eigenvector that is not invariant under lattice translations.

B. Branches 2 and 3

We followed a similar procedure in order to obtain the scaling dimensions X_t and X_h as for branch 1. The extrapolated results are shown in Table VI. The entries for X_t at $n = 1$ are shown to indicate that the temperaturelike energy gaps of finite systems diverge for $n \to 1$. However, this is due to another eigenvalue of the transfer matrix that obscures the true scaling behavior for small system sizes. If one would first take the limit $L \to \infty$ and then the limit $n \to 1$, a result $X_t \approx 2$ is expected. For $n = 1$, the finite-size results for the scaled magnetic gaps vanish, and the corresponding entry $X_h = 0$ is in line with the entries for branch 2 with $n > 1$.

For branch 2, a range $n \gtrsim 2$ exists where the scaled temperaturelike gaps decrease slowly with increasing L, but power-law fits in the range of accessible values of L do not suggest convergence. Only at much larger values of n does it become clear (see Table VI) that crossover occurs to a fixed point with a vanishing X_t.

TABLE VI. Numerical results for the temperature dimension X_t and the magnetic dimension X_h of the branch-2 and branch-3 models. Estimated numerical uncertainties in the last decimal place are given between parentheses.

n	X_t (branch 2)	X_h (branch 2)	X_t (branch 3)
1.0	∞	0 (−)	∞
1.2	2.0 (?)	0.00 (2)	0.8 (1)
1.4	1.9 (1)	0.04 (2)	1.0 (2)
1.6	1.90 (5)	0.08 (1)	1.4 (?)
1.8	2.00 (5)	0.105 (5)	1.6 (2)
2.0	1.9 (1)	0.122 (2)	0 (−)
10	−0.2 (2)	0.0 (1)	−0.1 (3)
20	0.0 (1)	0.0 (2)	0.0 (1)
30	0.00 (1)	0.000 (2)	0.00 (1)

A similar result is found for X_t on branch 3 at large n. However, for $n \to 2$ the behavior is different and the thermal scaled gaps of finite systems vanish in this limit.

The finite-size data for X_h on branch 2 with $n < 1.5$ could not be satisfactorily fitted with a power law. The assumption that $X_h(L) \simeq X_h + a/\ln L$ gave somewhat better behaved results, but the errors are hard to estimate. In Table VI we base the error estimates on the differences between the above logarithmic fits and fits with a fixed power −1. Also for $n = 2$ we used logarithmic fits, which yielded a best estimate not far from the exact value $X_h = 1/8$. In the case of branch 3, the free energies oscillate not only between even and odd systems, but also with a period four, and we did not produce meaningful estimates of X_h.

C. Branches 4 and 5

As noted in Sec. IV, the leading eigenvalues of the transfer matrices of finite branch-4 systems for $n > -2$ are equal to those for branch 5. Since this does not hold for the rest of the eigenvalue spectra, we perform separate analyses for the two branches. Unfortunately, the convergence of the scaled gaps is very poor, and we did not find accurate results. Power-law fits tend to yield finite-size exponents that vary considerably with system size, often assuming positive values. Logarithmic fits $X_t(L) \simeq X_t + a/\ln L$ were not very satisfactory either, because the finite-size data display an extremum as a function of the finite size for some values of n. Under these circumstances, we take the branch-4 scaled gaps at system size $L = 16$ as our final estimates. They are shown in Table VII. The difference with the result of the logarithmic fit, or 10 times the difference between the $L = 14$ and 16 results, is quoted as a rough estimate of the error margin.

A similarly slow convergence is observed for the branch-5 scaled gaps. For $n < -2$ we have the additional problem that the largest eigenvalues display a finite-size dependence not only with an odd-even alternation, but also with an effect of period 4. However, some observations can still be made. For large negative n the scaled gaps tend to become very small, and for n closer to −2 they are at most a few tenths, and tend to decrease with increasing L. For $n = -2$ the largest eigenvalues become degenerate, which corresponds with $X_t = 0$. The final estimates of X_t shown in Table VII for $n > -2$ are taken from logarithmic fits, and the error estimates are taken as their differences with the scaled gaps at $L = 14$. The entry at $n = 0$ is obtained from interpolation between small negative and positive values of n, because the vertex weight c/n in Eq. (3) diverges at $n = 0$. Similar numerical problems appear during analysis of the magnetic gaps as defined in Eq. (38). Thus, also the results for X_h in Table VII, and their error estimates, are somewhat uncertain.

TABLE VII. Fit results for the temperature dimension X_t and the magnetic dimension X_h of the branch-4 and branch-5 models. Estimated numerical uncertainties in the last decimal place are given between parentheses. The entries "0 (−)" indicate that the raw numerical data agree, up to numerical precision, with a vanishing result.

n	X_t (branch 4)	X_h (branch 4)	X_t (branch 5)	X_h (branch 5)
–8.0	2.3 (5)			
–4.0	2.3 (2)	–0.12 (5)		–0.8 (2)
–2.0	2.3 (2)	–0.09 (5)	0 (−)	–0.47 (5)
–1.8	2.3 (2)	–0.08 (5)	0.0 (1)	–0.43 (5)
–1.6	2.3 (2)	–0.08 (5)	0.0 (1)	–0.40 (5)
–1.4	2.3 (2)	–0.08 (4)	0.0 (1)	–0.37 (5)
–1.2	2.3 (2)	–0.07 (5)	0.0 (1)	–0.33 (5)
–1.0	2.3 (2)	–0.07 (5)	0.0 (1)	–0.30 (5)
–0.8	2.3 (2)	–0.06 (5)	0.1 (1)	–0.27 (5)
–0.6	2.2 (2)	–0.06 (4)	0.1 (2)	–0.24 (4)
–0.4	2.2 (1)	–0.05 (4)	0.1 (2)	–0.21 (4)
–0.2	2.2 (1)	–0.05 (3)	0.1 (2)	–0.17 (4)
0.0	2.2 (1)	–0.04 (3)	0.1 (3)	
0.2	2.2 (1)	–0.03 (3)	0.2 (3)	–0.11 (5)
0.4	2.2 (1)	–0.03 (3)	0.3 (3)	–0.08 (2)
0.6	2.2 (1)	–0.02 (2)	0.3 (3)	–0.05 (2)
0.8	2.2 (2)	–0.01 (2)	0.4 (3)	–0.02 (2)
1.0	2.1 (2)	0 (−)	0.5 (3)	0 (−)
1.2	2.0 (3)	0.013 (3)	0.7 (3)	0.02 (2)
1.4	2.0 (3)	0.03 (4)	0.9 (2)	0.054 (2)
1.6	1.9 (3)	0.05 (3)	1.1 (2)	0.07 (2)
1.8	1.8 (3)	0.07 (3)	1.5 (2)	0.09 (2)
2.0	1.7 (2)	0.11 (2)	1.9 (2)	0.11 (2)
4.0	1.4 (4)	0.5 (1)	1.3 (2)	0.125 (3)
8.0	1.5 (5)		1.4 (2)	0.12 (4)

VI. LOCATION OF PHASE TRANSITIONS

In order to explore the physical properties of the seven branches of solvable models described in Table I, we performed some further numerical work. Without aiming at a complete coverage of the phase diagram, we wish to investigate the possible association of the solvable branches with lines of phase transitions or the location of these branches with respect to such phase transitions.

For this purpose, we have calculated finite-size data for the scaled temperaturelike gap, using Eq. (36), and for the magnetic gap using Eq. (38), along lines in the phase diagram that intersect with the branches of interest.

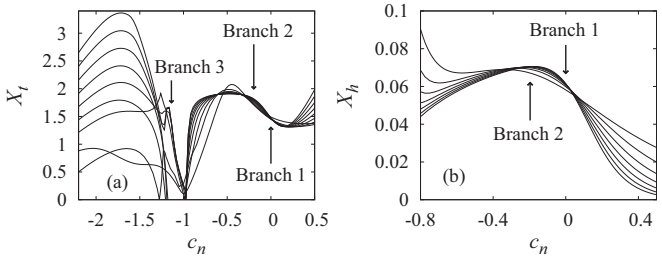

FIG. 4. Scaled thermal (a) and magnetic (b) gaps versus c_n covering branches 1, 2, and 3 of the completely packed O(n) loop model with $n = 1.5$. Results are shown for even system sizes $L = 4$ to 20 for the thermal case, and for $L = 4$ to 18 for the magnetic case. In panel (a) the scaled thermal gaps increase with L, on both the left and the right sides of the scale. Instead, in panel (b) the scaled magnetic gaps decrease on both sides. The data for X_t display cusps near $c_n \approx -1.2$, which are due to intersections between transfer-matrix eigenvalues. Complex pairs of eigenvalues then appear in a range of c_n for system sizes equal to odd multiples of 2. The corresponding data for these ranges are not shown in this figure.

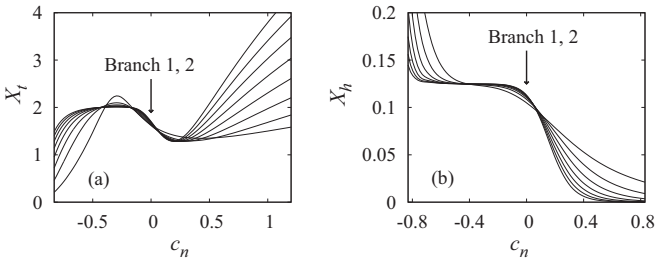

FIG. 5. Scaled thermal (a) and magnetic (b) gaps versus c_n covering branches 1 and 2 of the completely packed O(n) loop model with $n = 2$. Results are shown for even system sizes $L = 4$ to 18 for the thermal case and for $L = 4$ to 16 for the magnetic case. In panel (a) the scaled thermal gaps increase with L near $c_n = 1$, while the scaled magnetic gaps instead decrease on the right-hand end of the scale.

A. Branch 1

The completely packed nonintersecting O(n) loop model with $|n| < 2$ on the square lattice belongs to the same universality classes as the dense phase of the O(n) model. For the latter model, the introduction of crossing bonds, as well as that of cubic vertices, leads to crossover to different universal behavior. Both of these perturbations are described by the cubic-crossover exponent given by Eq. (30), which is relevant in the dense O(n) phase. Thus, branch 1 is a locus of phase transitions in the (n,x,c_n) parameter space, at least for $|n| < 2$. This was already illustrated for the dense O(n) phase by transfer-matrix calculations in Ref. [11]. For the present completely packed case, a few instances of the effect of a variation of the weights of the cubic and crossing-bond vertices on branch 1 will be included in the following sections treating branches 2–5.

B. Branches 2 and 3

For branches 2 and 3, only z-type and c-type vertices are present. These two branches exist only for $n \geqslant 1$. They merge at the end point $n = 1$, where the system reduces to a trivial case with effective weight 1 for each loop and each vertex. We first consider the thermal and magnetic scaled gaps X_t and X_h of a system with $n = 1.5$ as a function of c_n. Results are shown in Figs. 4. Several details can be noted. At $c_n = 0$, which is the location of branch 1, the scaled gaps are nicely approaching the values given by Eqs. (28). Furthermore, the curves for X_t show intersections close to the branch-1 point, with slopes that increase with L. Then a comparison with the scaling behavior expressed by Eq. (37), with y_t playing the role of the exponent of the cubic perturbation c_n, shows that the cubic perturbation is relevant on branch 1 at $n = 1.5$, because the slopes increase with L. Slightly to the left of branch 2, intersections occur as well, but here the cubic weight seems to be irrelevant. Indeed, for $c_n < 0$ there exists a range about branch 2 where the X_t data are consistent with slow convergence to a value close to 2, independent of c_n. The data for $c_n < -1$ appear to behave irregularly due to finite-size effects with a period exceeding 2. However, the data with L restricted to multiples of 4 allow convergence at the branch-3 point. The data with c_n smaller than the branch-3 value indicate that scaled gaps diverge with increasing L.

The results for X_h in Fig. 4(b) display a similar scaling behavior near branches 1 and 2. At $c_n = 0$ (branch 1) the data agree with convergence to the theoretical value given by Eq. (28). The slow apparent convergence for $c_n < 0$ indicates the existence of a marginal or almost marginal temperature dimension $X_t \approx 2$. In the neighborhood of branch 3, the X_h data (not shown) lose transparency because of the irregular finite-size dependence. For c_n significantly less than the branch-3 value, as well as for c_n significantly exceeding the branch-2 value, the data are consistent with convergence to $X_h = 0$, as expected for a phase dominated by cubic vertices.

For $n = 2$, $c_n > -2$, again one finds divergent behavior of the gaps X_t, corresponding with a noncritical phase dominated by c-type vertices. The same observation applies to the range where c_n considerably exceeds the branch-1 value. Again, complex eigenvalues occur near branch 3. The behavior of X_t and X_h in the neighborhood of branch 1, which coincides with branch 2 for $n = 2$, is shown in Figs. 5. These data indicate that there exists a range $c_n < 0$ where the cubic weight is marginal, for which $X_h = 1/8$ and $X_t = 2$.

Next we consider the thermal and magnetic scaled gaps in the range $n > 2$. Figure 6 shows these quantities for $n = 10$ as a function of the cubic weight $c_n = c/n$, for a range of system sizes, with z fixed at $z = 1$. The X_t curves are seen to display minima, which become increasingly pronounced for larger system sizes, and whose location rapidly converges to the branch-2 value $c_n = 0.2$. The X_h curves instead monotonically decrease as a function of c_n, and they intersect at points that rapidly approach the branch-2 value of c_n. Furthermore, extrapolation of the two types of scaled gaps at the minima or at the intersections leads to values close to 0 (see also Table VI), strongly suggesting a first-order phase transition at branch 2. The scaled magnetic gaps for c_n smaller than the branch-2 value in this figure seem to diverge, as expected for a disordered phase. Instead, for c_n exceeding the branch-2 value, the magnetic gaps rapidly approach zero, indicating a long-range-ordered phase in which the cubic vertices percolate. The divergent behavior of the scaled thermal gaps on either side of

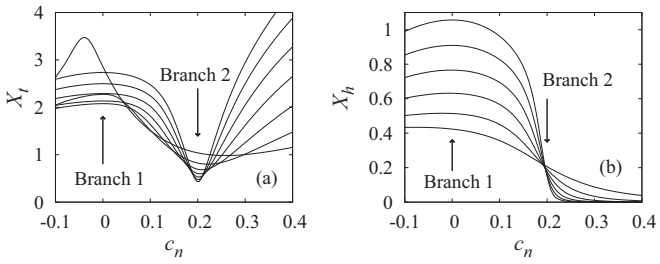

FIG. 6. Scaled thermal (a) and magnetic (b) gaps versus $c_n = c/n$ of the cubic-O(n) loop model with $n = 10$. The scaled gaps are represented by means of smooth curves connecting the numerical data points. Different system sizes correspond with separate curves. The thermal gaps are shown for even system sizes $L = 4$ to 16, and the magnetic ones for $L = 4$ to 14. The correspondence is such that, in the neighborhood of branch 2, steeper curves belong to larger L. The intersections, as well as the data taken at branch 2, seem to converge to a vanishing value of the scaled gaps, which indicates that a first-order transition occurs at branch 2.

the branch-2 value indicates a finite energy-energy correlation length, consistent with this phase behavior.

Similar data were computed for other values of n. For $n > 10$ the minima and intersections display even more rapid convergence to the branch-2 values, and the gaps tend to vanish more rapidly with increasing L. For $n < 10$ the picture becomes less clear, and for $n \gtrsim 2$ we are unable to see clear signs of a first-order transition from the available data. However, we cannot not exclude a weak first-order transition, and it is plausible that branch 2 is the locus of a first-order transition for all $n > 2$.

For larger values of n also the behavior of the scaled gaps near branch 3 can be resolved. This is illustrated by the X_t and X_h plots for $n = 40$ shown in Fig. 7 as a function of c_n. The scaled gaps extrapolate to a value close to 0 at the branch 2 and 3 points. For other values of c_n, the thermal scaled gaps display a divergent behavior. So do the magnetic scaled gaps in the range between branches 2 and 3. Outside this range, the magnetic gaps rapidly approach the value $X_h = 0$, which is as expected for a phase in which the c-type vertices dominate.

More detailed pictures of the scaled thermal gaps in the regions near the locations of branches 2 and 3 are shown in

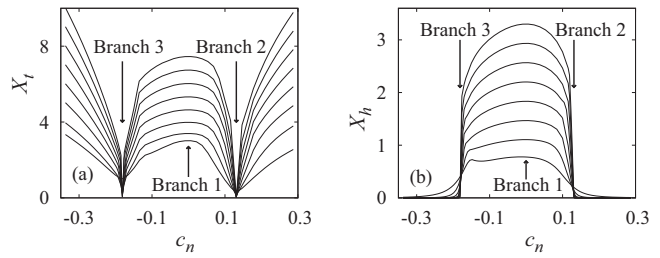

FIG. 7. Scaled thermal (a) and magnetic (b) gaps versus c_n covering branches 1, 2, and 3 of the completely packed O(n) loop model with $n = 40$. Results are shown for even system sizes $L = 6$ to 20 for the thermal case and for $L = 4$ to 18 for the magnetic case. In the middle part of the figures the scaled gaps increase with L.

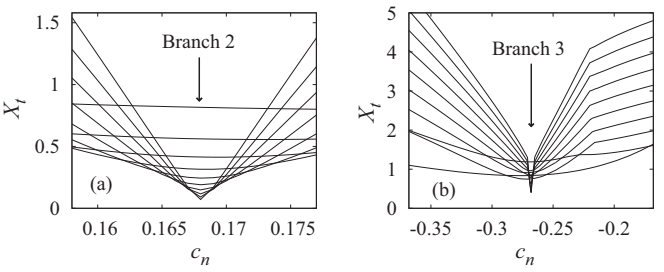

FIG. 8. Scaled thermal gaps versus c_n of the completely packed O(n) loop model with $n = 20$ around branch 2 in panel (a) and branch 3 in panel (b). Results are shown for even system sizes $L = 4$ to 22. The scaled gaps display, at branches 2 and 3, apparent convergence to 0 when L increases. Away from these transition points, they tend to diverge instead.

Fig. 8. These figures show data for $n = 20$ and include system sizes up to $L = 22$.

C. Branch 4

In the absence of cubic vertices for branch 4, we investigate of the phase behavior as a function of the crossing-bond weight, i.e., crossover phenomena between branch 1 and branch 4. The case of branch 5 involves all three vertex types and is treated separately. The results for the scaled thermal gaps, still denoted X_t, are obtained from a transfer matrix in an extended connectivity space, thus allowing for additional eigenvalues and associated scaling dimensions, in comparison with branch 1.

In Figs. 9 and 10, we present diagrams describing the scaling behavior of the thermal gaps as a function of x near branch 4 for $n = 0$ and 1 and $n = 2$ and 3, respectively. For $n = 0$ and 1, there are intersections close to $x = 0$, and the behavior of the slopes confirms that x is relevant, which tells us that a continuous phase transition takes place here. It is noteworthy that, for $n = 1$, the free energy is a trivial nonsingular function of the summed vertex weights. Thus, the phase transition at $x = 0$ can, for $n = 1$, only apply to the geometric properties of the loop configurations. Indeed, the intersections indicate

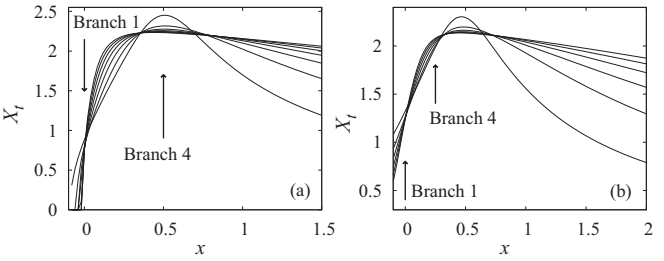

FIG. 9. Scaled thermal gaps versus the crossing-bond weight of the completely packed O(n) loop model around branch 4, for $n = 0$ in panel (a) and for $n = 1$ in panel (b). The location of branch 4 is indicated. Results are shown for even system sizes $L = 4$ to 16. The scaled gaps increase as a function of L for large x. The intersections of the curves near $x = 0$ agree well with the value $X_t = 3/4$ for cubic crossover in the dense phase of the $n = 0$ loop model, and with $X_t = 5/4$ for the $n = 1$ model.

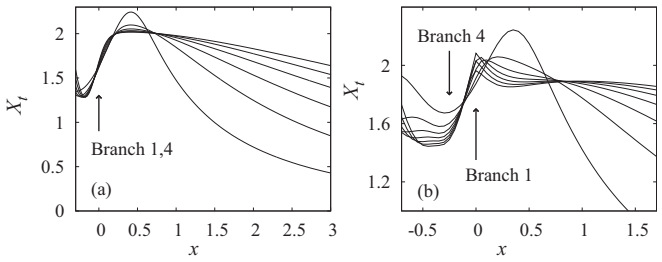

FIG. 10. Scaled thermal gaps versus the crossing-bond weight of the completely packed O(n) loop model around branch 4, for $n = 2$ in panel (a) and for $n = 3$ in panel (b). The location of branch 4 is indicated. Results are shown for even system sizes $L = 4$ to 16. The scaled gaps increase as a function of L for large x.

that $X_t = 5/4$ at the transition, corresponding with the thermal scaling dimension of the percolation critical point. For $n = 2$, the scaled gaps in the range $x > 0$ display a behavior consistent with marginal behavior as a function of x. Also in Fig. 10(b) for $n = 3$ one observes hints of marginal behavior for $x > 0$. For $x < 0$ there is a range where the scaled gaps are suggestive of another critical phase with a smaller dimension X_t.

The behavior of the scaled magnetic gaps, shown in Figs. 11 for $n = 0$ and 2, is consistent with that of X_t. Intersections are found for $n = 0$ near branch 1, rapidly converging to the expected value $X_h = -3/16$. Crossover to much smaller absolute values of X_h occurs for $x > 0$. For $n = 2$ the crossing-bond weight seems marginal, and in a range $x > 0$ one observes apparent convergence to an x-dependent value, thus indicating "nonuniversal" behavior.

One may expect that the introduction of crossing-bond-type vertices in the completely packed nonintersecting loop model with large n will affect the checkerboardlike ordering of the elementary loops. Thus, we numerically investigate the scaled gaps as a function of x for $n = 20$ in order to address the question whether a phase transition occurs as a function of the crossing-bond weight x. The results for X_t and X_h are plotted in Figs. 12. The X_t curves do have some intersections, but only involving the smallest system size. They do not provide evidence for an Ising-like transition where the checkerboard-like order of the $x = 0$ model vanishes. However, if, as the results in Sec. IV C suggest, the branch-4 model is in a critical state at $n = 20$, while the branch-1 model (at $x = 0$) is off-

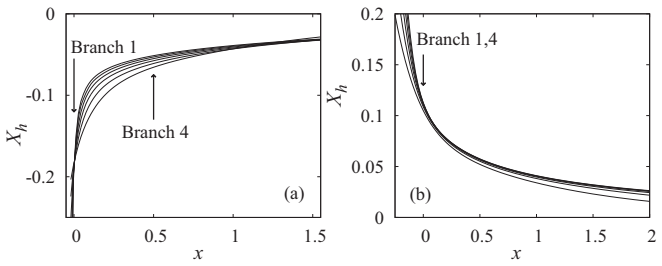

FIG. 11. Scaled magnetic gaps versus the crossing-bond weight of the completely packed O(n) loop model around branch 4, for $n = 0$ in panel (a) and for $n = 2$ in panel (b). The location of branch 4 is indicated. Results are shown for even system sizes $L = 4$ to 14. The scaled gaps increase as a function of L at branch 4.

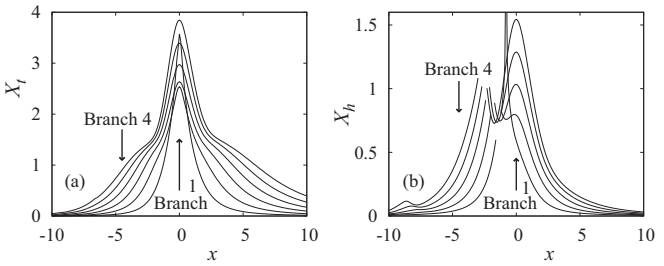

FIG. 12. Scaled thermal (a) and magnetic (b) gaps versus the crossing-bond weight of the completely packed O(n) loop model with $n = 20$. The thermal gaps are shown as separate curves for even system sizes $L = 4$ to 14 and the magnetic gaps for $L = 4$ to 12. Larger scaled gaps correspond with larger L in most of the range of the x scale. The missing parts in the X_h curves correspond with a level crossing of the leading eigenvalues of the odd systems that appear in Eq. (38). The intersections in the X_h curves occur close to the level crossing. The absence of intersections between the X_t curves for $L > 4$ indicates that there is, at most, a weakly singular phase transition as a function of x.

critical, then there must be a transition of some kind. Perhaps the "shoulder" that develops in the curves near $x = -3$ is a sign of a weak transition. A similar shoulder is present in the physical range $x > 0$. We note that, while the results at $x = 0$ in Fig. 12 increase rapidly with L, the results near the shoulders seem consistent with convergence to a finite value of X_t. The data for X_h do display intersections for $x < 0$, close to a crossing of the leading transfer-matrix eigenvalues of odd systems, involving a doublet and a singlet. For positive x the singlet is the largest eigenvalue.

D. Branch 5

The analysis of the phase behavior in the neighborhood of branch 5 is somewhat more involved in the sense that we now have all three types of vertices in the system. Due to the larger number of connectivities for a given system size, the calculations for branch 5 are restricted to smaller systems than those for branch 4. We investigate the influence of a variation of x as well as of c_n.

1. Variation of the crossing-bond weight

The scaled thermal gaps for $n = 0$ and 1 are shown in Figs. 13 as a function of the crossing-bond weight x, while the cubic weight c_n is kept at its branch-5 value. Although the partition sum remains well behaved, the cubic weight as used in the transfer-matrix calculations diverges at $n = 0$. Therefore, the thermal gaps for $n = 0$ were obtained by averaging those for $n = \pm 0.05$. The resulting thermal gaps for $n = 0$ display intersections near branch 5, and the two corresponding eigenvalues of the transfer matrix merge into a complex pair at values of x that are only slightly smaller. For $n = 1$, there are also intersections near branch 5, approaching the branch-5 point when L increases.

At the intersections, the slopes of the curves increase with L, which indicates that the crossing bonds are relevant at branch 5 and thus induce a phase transition. For $n = 1$, this

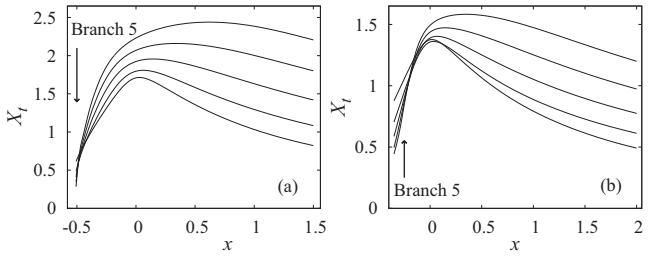

FIG. 13. Scaled thermal gaps versus the crossing-bond weight of the completely packed O(n) loop model around branch 5 for $n = 0$ in panel (a) and for $n = 1$ in panel (b). The cubic weight is fixed at its value at branch 5. Results are shown for even system sizes $L = 4$ to 12. The scaled gaps increase as a function of L on the right-hand side.

transition may describe some geometric property of the graph configurations.

In Figs. 14 we show the scaled gaps as a function of x for $n = 2$ and 3. For $n = 2$, a cusp appears at the branch-5 point, which is due to an intersection of the second and third eigenvalues of the transfer matrix. The curves are suggestive of "nonuniversal" behavior of X_t when x is varied. Note that, although branches 4 and 5 coincide at $n = 2$, the cusps are absent in Fig. 10(a). This is due to the fact that, for $x > 0$, the subleading thermal eigenvalue for branch 5 is absent for branch 4, whose transfer matrix acts in a smaller configuration space. For $x \leqslant 0$, Figs. 10(a) and 14(a) match exactly. The curves for $n = 3$ in Fig. 14(b) display some structure superimposed on marginal-like behavior, which may, however, be due to slow crossover effects as may be expected for $n \gtrsim 2$.

We also include results for the thermal and magnetic gaps for $n = 10$ and 20 in Figs. 15 and 16. The magnetic gaps were calculated on the basis of Eq. (38). The scaling behavior of the results for even L is consistent with that for odd L, but there is some alternation effect. We show the magnetic gaps only for odd L. The results for $n = 10$ still seem consistent with convergence to nontrivial values $X_t \approx 3/2$ and $X_h \approx 1/8$. For $n = 20$ this is even less clear. A pronounced difference between $n = 10$ and 20 is seen in the X_h plots near $x = 0$, where the magnetic gaps for $n = 20$ rapidly approach 0 with

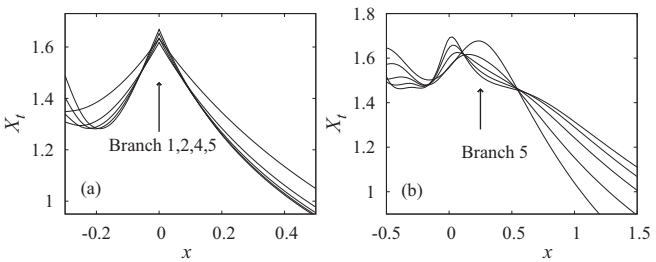

FIG. 14. Scaled thermal gaps versus the crossing-bond weight of the completely packed O(n) loop model around branch 5 for $n = 2$ in panel (a) and for $n = 3$ in panel (b). The cubic weight vanishes for $n = 2$ at branch 5. This is precisely the intersection point of branches 1, 2, 4, and 5. Results are shown for even system sizes $L = 4$ to 12. The cusps at $x = 0$ are due to intersections between the second and third eigenvalues of the transfer matrix. For $n = 2$, the scaled gaps decrease as a function of L on the right-hand side; for $n = 3$, they increase.

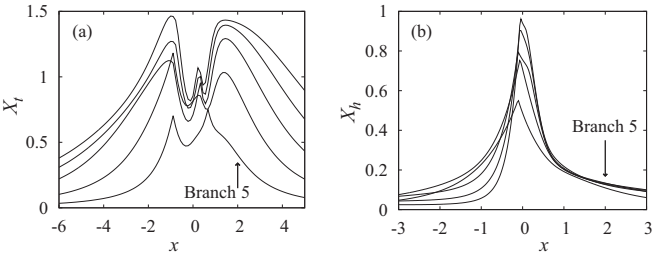

FIG. 15. Scaled gaps versus the crossing-bond weight of the completely packed O(n) loop model around branch 5 for $n = 10$. The thermal gaps are shown in panel (a) for even $4 \leqslant L \leqslant 12$ and the magnetic gaps in panel (b) for odd $3 \leqslant L \leqslant 11$. The cubic weight is fixed at its branch-5 value. The scaled gaps increase as a function of L in the neighborhood of branch 5. However, for X_h, $x < 0$ they tend to become smaller instead.

increasing L, thereby revealing a phase dominated by cubic vertices. The sharp extrema for $n = 20$ near $x = 2$ may be associated with a transition between a phase with mainly c-type vertices and one with x-type vertices.

2. *Variation of the cubic vertex weight*

We also investigated the behavior of the system near branch under a change of c_n. Figures 17 display the results for the scaled thermal gap for $n = 0$ and $n = 1$. Those for $n = 0$ are again obtained by interpolation between $n = -0.05$ and 0.05. The intersections indicate that a continuous phase transition takes place at branch 5. At cubic vertex weights somewhat smaller than the branch-5 value one finds complex eigenvalues, similar to the situation found when x becomes smaller with respect to its branch-5 value; see Figs. 13. The apparent divergence of the scaled gaps for larger values of the cubic vertex weight indicates a noncritical state dominated by c-type vertices.

The X_t data for $n = 2$ are shown in Figs. 18. The point $c_n = 0$ is the intersection of branches 1, 2, 4, and 5. For $c_n > 0$, the scaled gaps again display a divergent behavior. Although the vector space of the transfer matrix for branch 5 is larger than for branch 2, the X_t data coincide with those in Fig. 5(a) in this range. Different behavior occurs for $c_n > 0$.

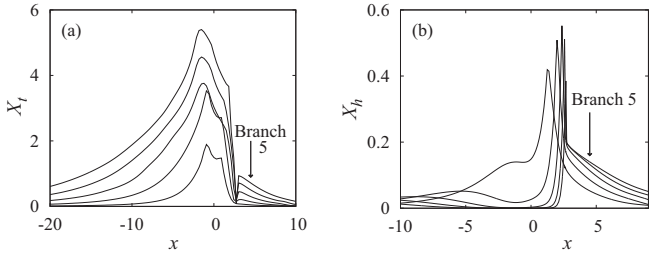

FIG. 16. Scaled gaps versus the crossing-bond weight of the completely packed O(n) loop model around branch 5 for $n = 20$. The thermal gaps are shown in panel (a) for even $4 \leqslant L \leqslant 12$, and the magnetic gaps in panel (b) for odd $3 \leqslant L \leqslant 11$. The cubic weight is fixed at its branch-5 value. The scaled gaps increase as a function of L near branch 5. However, for X_h, $x < 0$ there exists a range where they tend to 0 instead.

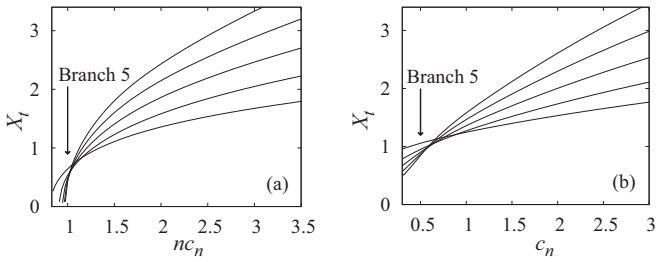

FIG. 17. Scaled thermal gaps versus the cubic vertex weight of the completely packed O(n) loop model around branch 5 for $n = 0$ in panel (a) and for $n = 1$ in panel (b). The crossing-bond weight x is fixed at its branch-5 value. Results are shown for even system sizes $L = 4$ to 12. The scaled gaps increase as a function of L on the right-hand side. The branch-5 cubic vertex weight c_n diverges at $n = 0$, but $c = nc_n$ (horizontal scale) remains finite.

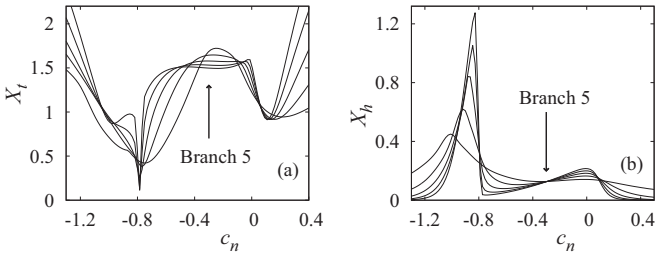

FIG. 19. Scaled gaps versus c_n of the completely packed O(n) loop model around branch 5 with $n = 5$. Panel (a) shows the data for X_t and panel (b) shows the data for X_h. The crossing-bond weight is fixed at its value at branch 5. Results are shown for odd L in the range $3 \leqslant L \leqslant 11$. The scaled thermal gaps at branch 5 decrease as a function of L, while the magnetic gaps display intersections near branch 5; there, the steeper curves correspond with larger L.

The X_t data no longer agree with those in Fig. 5(a) and display a "nonuniversal" range $c_n < 0$ where the thermal scaling dimension X_t depends continuously on c_n. The difference with the corresponding branch-2 data for X_t is due to the second-largest eigenvalue for branch 5. The largest eigenvalues are the same for both branches at $n = 2$; thus, the behavior of the magnetic gaps for branch 5 is the same as shown in Fig. 5(b).

Finally, we display the effect of a change of the cubic vertex weight on the branch-5 systems with $n = 5$ and 10. The corresponding scaling plots are shown in Figs. 19 and 20. These results may suggest convergence to a nontrivial temperature dimension $X_t \approx 1.5$, in a range of c_n about branch 5, but again we have to consider the possibility of strong crossover phenomena. The sharp minima near $c_n = -0.7$ tend to $X_t = 0$ and thus suggest a first-order transition to a state dominated by c-type vertices. Instead, the intersections of the curves near $c_n = 0$ tend to a nonzero value, corresponding to a continuous transition to a c-dominated phase.

Our numerical results for $n = 30$ (not shown) are entirely consistent with this picture. There are sharp minima in the X_t curves near $c_n = -0.6$ and $c_n = 0$. In between, the data increase slowly with L, up to a maximum of about $X_t = 0.6$ for $L = 12$, but do not allow a firm conclusion about their convergence. Outside this range, the scaled gaps clearly display divergent behavior as expected for off-critical phases dominated by the c-type vertices.

VII. DISCUSSION

We have investigated the completely packed Eulerian graph model on the square lattice with three types of vertices. In particular, we focused on the symmetric case with vertex weights satisfying the fourfold rotational symmetry of the lattice. We explored the physics associated with the exactly solvable cases of the equivalent Perk-Schultz coloring model. We have checked and extended the results for the bulk free energy given by Schultz [14] for the symmetric cases of the coloring model. We also explored the phase diagram in the neighborhood of branches 1 to 5, which revealed many details concerning the nature of the relevant phases and their transitions.

Branch 1. This model (or its equivalent models) has already been studied extensively and there are well-established results. We investigated the equivalence of two seemingly different solutions applying to the case $n > 2$ case analytically. Indeed, we found that the Schultz solution for the partition sum per site for $n > 2$ is exactly equivalent with the Baxter solution for

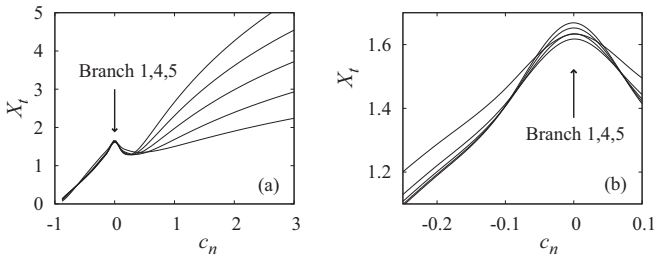

FIG. 18. Scaled thermal gaps versus the cubic vertex weight of the completely packed O(n) loop model around branch 5 for $n = 2$. The scaled gaps for $c_n < 0$ are hard to distinguish in panel (a); an enlarged view is shown in panel (b). The cubic weight is fixed at its value at branch 5. Results are shown for even system sizes $L = 4$ to 12. The scaled gaps increase as a function of L on the right-hand side of panel (a), and they decrease on the left-hand side of panel (b).

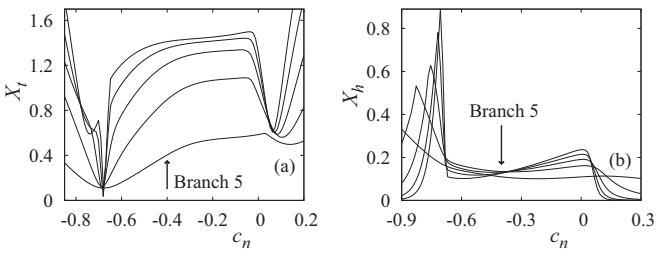

FIG. 20. Scaled gaps versus c_n of the completely packed O(n) loop model around branch 5 with $n = 10$. Panel (a) shows the data for X_t and panel (b) shows the data for X_h. The crossing-bond weight is fixed at its value at branch 5. Results are shown for odd L in the range $3 \leqslant L \leqslant 11$. The scaled thermal gaps at branch 5 increase as a function of L, while the magnetic gaps display intersections near branch 5; there the steeper curves correspond with larger L.

the $q > 4$-state Potts model, and thus with the corresponding range of the Lieb solution of the six-vertex model.

We also checked the consistency between the analytic solutions and our numerical results for the free energy. We find accurate agreement with the Baxter solution for the Potts model, which applies to the range $n > 0$, and with the Lieb solution [24], which is specified for all $n > -1$. The latter solution is also valid down to $n = -2$. Furthermore, the continuation of the Lieb solution to complex parameters [26], which covers the range $n < -2$, agrees precisely with our numerical free-energy results for that range of n.

We also compared our numerical results for the scaling dimensions with the Coulomb gas predictions for $|n| < 2$, and found a satisfactory agreement. Our numerical results show that a temperaturelike scaling dimension $X_{t1} = 4$ exists, which is the leading dimension of that type for $n < 1$.

Branch 2. The Schultz solution for the partition sum of this branch proved to be consistent with our transfer-matrix analysis. The latter calculations benefited from an improved coding algorithm (see the Appendix) that allowed us to reach larger system sizes in comparison with Ref. [11].

The physical character of this model, which includes z-type as well as c-type vertices, depends on the range on n. For $n > 2$, branch 2 is physical in the sense of positive Boltzmann weights. For large system sizes, the scaled gaps approach a value consistent with 0, indicative of a first-order phase transition. Furthermore, the exploration of the phase diagram of the model as a function of the cubic vertex weight, reported in Sec. VI, indeed shows that, at least for $n \gg 2$, branch 2 corresponds with a locus of first-order phase transitions. As for the nature of this transition, we recall that for $x = c = 0$ (branch 1) the system displays a checkerboardlike order. This order can break down when vacant vertices are introduced [43], and it is plausible that the introduction of cubic vertices will yield a similar result. Concerning the physical reason behind the first-order nature, we mention that the transition is located at a cubic weight $c \approx \sqrt{n}$ for large n. That is where the Boltzmann weights of the checkerboard O(n) phase and that of the fully ordered cubic phase coincide. There, the introduction of a cubic vertex in the checkerboard background of z-type vertices increases the Boltzmann weight by a factor $\sqrt{n}$, but the number of components in Eq. (1) decreases by one, which costs a factor n. Furthermore, two or three cubic vertices do not interact. Only when four cubic vertices form a square is there no factor $1/n$ involved in the addition of the last vertex. For this reason, there is no appreciable attraction between the cubic vertices when their density $\rho = N_c/N$ is low. As long as the density is small, it is thus mainly governed by the fugacity c_n of the cubic vertices, since we have set $z = 1$ in Eq. (1).

Let us next consider the attraction between the cubic vertices when their density is no longer negligible, using a mean-field-type approximation. For this purpose we denote the absence or presence of a cubic vertex on site i by means of a site variable σ_i with corresponding values $\sigma_i = 0$ and 1, respectively. Due to the absence of a factor $1/n$ when four cubic vertices form a square, the above-mentioned weight c_n of a cubic vertex has to be replaced with $(c_n)[n\rho^3 + 1 - \rho^3]$. Thus, the mean-field self-consistency equation at low densities

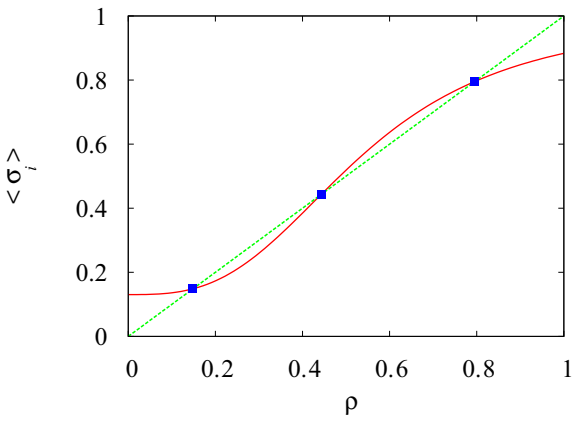

FIG. 21. (Color online) Mean-field approximation for the density of the type-c vertices, for $n = 100$ and $c_n = 3/40$. The existence of three solutions (square symbols) for this density is a sign of a first-order transition.

of the cubic vertices becomes

$$\langle \sigma_i \rangle = \frac{(n-1)\rho^3 + 1}{(n-1)\rho^3 + 1 + 1/c_n}. \tag{44}$$

A self-consistent solution of the equation $\rho = \langle \sigma_i \rangle$ for large n exists with ρ not exceeding a value of order $1/\sqrt{n}$, as long as c_n does not exceed $\sqrt{n}$, near the locus of the phase transition. This smallness of ρ is already a sign that the phase transition for large n is first order. Numerical evaluation of $\langle \sigma_i \rangle$ for large n, $c_n \approx \sqrt{n}$ indeed shows three solutions of the equation $\langle \sigma_i \rangle = \rho$, corresponding with a jump in ρ when c_n is varied. An example is given in Fig. 21 for $n = 100$ and $c_n = 3/40$. The curve shows Eq. (44), and the straight line shows the self-consistency condition $\langle \sigma_i \rangle = \rho$.

For $n < 2$, the cubic weight at branch 2 becomes negative, but the model is not necessarily unphysical, since its weights in the equivalent coloring-model representation are non-negative. Furthermore, the sign of a cubic perturbation is important in the context of the universal behavior of the O(n) spin model. Depending on this sign, crossover will occur to the face-cubic or to the corner-cubic phase. From the association of the face-cubic model with four-leg vertices [8] one may interpret a negative cubic vertex weight with crossover to a corner-cubic state. Indeed, the cubic perturbation is relevant in the dense O(n) loop phase according to the theory [10] and numerical work [11]. The cubic weight is rather limited for branch 2 with $1 < n < 2$, in line with the physical association with a low-temperature corner-cubic state.

Branch 3. Also our numerical results for the free energy of branch 3 are in a good agreement with the exact result of Schultz [14]. The data presented in Sec. VI indicate that also branch 3 is the locus of a first-order transition line in the n versus c_n phase diagram for sufficiently large n. Just as for branch 2, the transition can be interpreted as the frontier of the long-range ordered lattice-gas-like state that occurs when the z-type vertex dominates. The scaling behavior of the gaps is, for large n, similar to that of branch 2. The loop-model version of the branch-3 model is, however, unlike branch 2, unphysical for all n, because the cubic weight c_n is negative. However,

the coloring-model weights are still positive for $1 < n < 2$. In that range, the numerical results for the conformal anomaly seem to diverge, and the scaled gaps at branch 3 display poor convergence with L and do not allow a satisfactory estimation of the scaling dimensions. However, it is clear that a range of c_n exists between branches 2 and 3, where X_t tends to converge to a c_n-independent value close to 2, which suggests that an algebraic phase exists. It does still seem well possible that branch 3 defines the boundary of that phase.

Branch 4. In this case, both z-type and x-type vertices are present. An analysis of the difference between the expressions given by Schultz [14] and Rietman [29] in Sec. II C 3 showed that the Schultz result has to be modified with a factor $\mathrm{ctg}(\alpha\pi)$, after which it becomes equivalent with the Rietman result. This factor specifies the periodic function $p(s)$ mentioned in footnote 64 of Ref. [15], which refers to Ref. [14]. Indeed, the numerical analysis presented in Sec. IV is in a good agreement with the Rietman solution [29] for $n \leqslant 2$. The latter solution does not apply to the range $n > 2$. On the basis of our transfer-matrix results we conjecture that the free energy is symmetric with respect to $n = 2$, i.e., $f(n)$ satisfies $f(2 + x) = f(2 - x)$. This generalizes the Rietman result to an expression for the free energy per site for all n, listed in Eq. (40).

Our numerical estimates of the conformal anomaly c_a for $n \leqslant 2$, although not accurate, confirm the existing result [9] $c_\mathrm{a} = n - 1$. For $n \geqslant 2$ our results allow the conjecture $c_\mathrm{a} = n/2$. The results for the scaling dimensions for branch 4 with $n < 2$ in Table V are mildly suggestive of $X_t = 2$ and $X_h = 0$,

Concerning the phase diagram of the intersecting O(n) loop model, thus the system described by Eq. (1) with $c = 0$ and x/z and n as variable parameters, we find different types of behavior in the ranges $n > 2$ and $n < 2$. For $n \gg 2$ we see no evidence of a strongly singular transition as a function of x. However, the lattice-gas-like order that exists for $x = 0$ should dissolve when the z-type vertices become sparse for larger x, and thus a phase transition of a weak signature seems very likely.

For $n < 2$, the dense phase of the nonintersecting loop model still displays Ising-like ordering, but here the introduction of crossing-bond (x-type) vertices is a relevant perturbation. It is, just as the cubic perturbation, described by a four-leg vertex, for which the Coulomb gas analysis [10] can be applied, which then yields the exact scaling dimension of this perturbation. Its relevance for $n < 2$ leads to different universal properties of the dense phase of the model with crossing bonds in comparison with those of the nonintersecting loop model [9,11]. Indeed, we observed such crossover to different universal behavior in Sec. VI when a nonzero weight x is introduced. It is noteworthy that, for $x = 0$, the leading temperaturelike dimension X_t assumes a value corresponding with the cubic-crossover exponent given by Eq. (30), different from the corresponding result in Table V. It thus reflects that the enlargement of the set of connectivities, caused by the introduction of crossing bonds, allows the coding of more correlation functions in comparison with the nonintersecting subset.

Our analysis of the scaled gaps and the associated scaling dimensions as a function of the crossing-bond weight, while the weight of the nonintersecting vertices is kept constant, confirmed that a phase transition takes place at $x = 0$ for $-2 < n < 2$. For $x > 0$, we did not find clear signs of a phase transition for any value of n, in contrast with the findings reported in Ref. [11]. The latter work does, however, not concern completely packed systems.

Branch 5. The identity of the free energy of branches 4 and 5 can be understood by translating the generalized loop model back into coloring-model language. According to Eq. (11) and Table I, both W^d and W^r take the same values for branch 4 as for branch 5. The weight W^0 has different signs for the two branches, but the absolute values are the same. Furthermore, the weight W^0 describes the crossing of loops of a different color, and the number of such intersections must be even in the even systems that we are considering. Therefore, the free energy, and the largest eigenvalue of the transfer matrix as well, must be the same for the two branches. Thus, we may still use the generalized Rietman result as the theoretical prediction of the free energy of the branch-5 model.

The transfer-matrix analysis for branch 5 is somewhat more involved than in the previous cases, since there are now three different types of vertices in the system. New eigenvalues appear in the configuration space of the transfer matrix, and the leading scaling dimensions of branch 5 are different from branch 4. The temperature exponent appears to be very small for $n < 2$, and the magnetic exponent seems to be negative.

A complete analysis of the phase behavior in a vicinity of branch 5 would involve the scanning of the 3D phase diagram parametrized by (x,c_n,n). Concerning this matter, we only performed superficial exploration in the $x - n$ diagram with the cubic weight fixed at its branch-5 value and in the $c_n - n$ diagram at a similarly fixed crossing-bond weight. In the $x - n$ diagram, no signs of phase transitions emerged in the immediate neighborhood of branch 5 for sufficiently large n ($n > 10$), but a transition to a c_n-dominated phase is seen at small x. For $n = 2$ there is a clear change of behavior at $x = 0$, where several branches intersect. On both sides of this point there is a "nonuniversal" range of x. For $n < 2$ the data show a transition at or near branch 5.

Similarly, in the $c_n - n$ diagram, a critical transition occurs at the location of branch 5 for $n < 2$. Our results indicate the existence of cubic long-range order when c_n exceeds its branch-5 value. For $n = 2$ there is again a clear "nonuniversal" range, but only for $c_n < 0$. For $c_n > 0$, the divergent behavior of X_t indicates the existence of a phase where the cubic vertices percolate, except perhaps in a small range close to $c_n = 0$. Also for $n \gg 2$ we observe phase transitions to the cubic phase, at both positive and larger negative values of c_n. In between, there seems to exist a phase where the scaling dimensions depend continuously on c_n.

Branch 6. Branch 6 is a very simple case with only one nonzero vertex weight, namely the crossing-bond or x type. Indeed, the Schultz solution predicts a trivial free-energy density. This agrees well with the largest transfer-matrix eigenvalues which are, according to Eq. (42), equal to

$$\Lambda_0(n,L) = n. \tag{45}$$

This result follows immediately from the vertex weights $n_z = n_c = 0$, $x = 1$ and Eq. (A4). Every new row added by the transfer matrix forms a loop closed about the cylinder, and thus contributes a factor n to the partition sum. The transfer matrix is diagonal, with all elements and eigenvalues equal to n.

Branch 7. This case is similar to that of branch 6, and again the Schultz solution predicts a trivial free-energy density, in agreement with our transfer-matrix results. Equation (43) implies the following eigenvalues:

$$\Lambda_0(n,L) = \begin{cases} n, & \text{if } L \text{ is even.} \\ n-2, & \text{if } L \text{ is odd.} \end{cases} \tag{46}$$

This result can be explained using the language of the coloring model, for which we only have nonzero vertex weights $W^0 = 1$ and $W^{\rm d} = -1$. Thus, all edges on a line in the transfer direction have the same color, and the same holds for edges on lines in the perpendicular direction. The weight of a newly added row depends on the colors of the lines in the transfer direction. The maximum weight is realized for L lines of the same color. The weight of a newly added row is 1 if it has one of the $n-1$ different colors and $(-1)^L$ if it has the same color. These weights indeed sum up to the multiplicities n and $n-2$ appearing in Eq. (46).

Finally, we remark that the present explorations, although yielding a lot of new information, are necessarily far from complete. Furthermore, the limited ranges of accessible finite sizes in our transfer-matrix analyses did, in several cases, not allow the derivation of satisfactorily accurate results. Perhaps Monte Carlo methods will be found to be helpful to resolve some of these issues.

ACKNOWLEDGMENTS

It is a pleasure to acknowledge valuable comments by and enlightening discussions with Professor B. Nienhuis and Professor J. H. H. Perk. This work was supported in part by the NSFC (China) under Grant No. 11175018 (W.G.) and by the Lorentz Fund.

APPENDIX: TRANSFER-MATRIX TECHNIQUE

A crucial piece of information for the construction of the transfer matrix for the generalized loop model is the way in which the dangling bonds at the end of the cylinder are mutually connected via some path of bonds in the cylinder. This information is called "connectivity," denoted by greek symbols α or β, etc. Let there be in total C_L possible connectivities for L dangling bonds. The partition sum $Z^{(M)}$ of a cylinder consisting of M circular rows of L vertices is divided into C_L restricted sums, according to the connectivity β of the dangling bonds. The restricted sums for the model of Eq. (3) are formally expressed as

$$Z_\beta^{(M)} = \sum_{\mathcal{G}_M} \delta_{\beta\varphi(\mathcal{G}_M)} z^{N_z} c_n^{N_c} x^{N_x} n^{N_l}, \tag{A1}$$

where φ is the connectivity implied by the Eulerian graph $\mathcal{G}_M$. Let us now add another row of L vertices and rewrite the restricted partition sums of the $(M+1)$-row system as

$$\begin{aligned} Z_\beta^{(M+1)} &= \sum_{\mathcal{G}_{M+1}} \delta_{\beta\varphi(\mathcal{G}_{M+1})} z^{N'_z} c_n^{N'_c} x^{N'_x} n^{N'_l} \\ &= \sum_{\mathcal{G}_M} z^{N_z} c_n^{N_c} x^{N_x} n^{N_l} \sum_{g_{M+1}} \delta_{\beta\varphi(\mathcal{G}_M, g_{M+1})} z^{n_z} c_n^{n_c} x^{n_x} n^{n_l(\alpha)}, \end{aligned} \tag{A2}$$

where the primed quantities refer to the $M+1$-row system, $\mathcal{G}_{M+1} = \mathcal{G}_M \cup g_{M+1}$, where g_{M+1} is the vertex configuration on the $M+1$th row, and the lowercase symbols n_z, n_c, n_x, and n_l denote the increase of the numbers of vertices and loops caused by the addition of the $(M+1)$th row. All these numbers depend on g_{M+1}, but only n_l depends also on α, the dependence of which is explicitly shown. Next, we note that the connectivity $\varphi(\mathcal{G}_{M+1})$ depends only on $\varphi(\mathcal{G}_M)$ and g_{M+1} and insert an innocent factor $\sum_{\alpha=1}^{C_L} \delta_{\alpha\varphi(\mathcal{G}_M)}$, which yields

$$\begin{aligned} Z_\beta^{(M+1)} = \sum_{\alpha=1}^{C_L} \sum_{\mathcal{G}_M} \delta_{\alpha\varphi(\mathcal{G}_M)} z^{N_z} c_n^{N_c} x^{N_x} n^{N_l} \\ \times \sum_{g_{M+1}} \delta_{\beta\varphi(\alpha, g_{M+1})} z^{n_z} c_n^{n_c} x^{n_x} n^{n_l(\alpha)}. \end{aligned} \tag{A3}$$

With the definition of the transfer-matrix elements by

$$T_{\beta\alpha} = \sum_{g_{M+1}} \delta_{\beta\varphi(\alpha, g_{M+1})} z^{n_z} c_n^{n_c} x^{n_x} n^{n_l(\alpha)}, \tag{A4}$$

Eq. (A3) assumes the recursive form

$$Z_\beta^{(M+1)} = \sum_{\alpha=1}^{C_L} T_{\beta\alpha} Z_\alpha^{(M)}. \tag{A5}$$

Repeated application yields that, in the large-M limit, the largest eigenvalue Λ_0 of the transfer matrix determines the free-energy density. In actual calculations, we do not explicitly compute the elements $T_{\beta\alpha}$, but the transfer-matrix is decomposed [4,40] instead in L sparse matrices, for which the required memory is only proportional to the number of connectivities, instead of quadratic.

1. Coding and decoding of the connectivities

For actual calculations one needs to determine the number C_L of L-point connectivities of the model and to code each of these by consecutive and unique integers $1,2,3,\ldots,C_L$. A decoding algorithm is needed as well. The numbers C_L increase with L, but in a way that still depends on the set of allowed vertices. Since it is, for the finite-size analysis, desirable to have as wide as possible ranges of system sizes L available for each parameter choice, we have constructed separate coding algorithms for four applicable sets, namely including z, z and x, z, and c, and, last, z, x, and c.

2. Some remarks on the actual coding methods

The existing literature already contains much information about the coding and decoding algorithms used in transfer-matrix calculations. Here we present only a short characterization of, or references to, the coding methods used in the present work. We first consider the case of even L, such that connected dangling bonds occur only in even numbers.

a. $x = c = 0$, $z \neq 0$

The coding of the z-type connectivities is part of a more complicated problem that was already described in some detail in Ref. [4], namely the coding of so-called dilute well-nested O(n) connectivities, which contain, besides connected pairs, also "vacant" dangling bonds, which are not occupied by a

loop segment. This is the coding method used for the case $z \neq 0, c = x = 0$.

b. $c = 0, z \neq 0, x \neq 0$

For intersecting loop models in which also x is nonzero, the connectivities are represented by rows of integers occurring in pairs, but no longer well-nested. The enumeration of these connectivities is described in Ref. [11].

c. $x = 0, z \neq 0, c \neq 0$

The coding problem for the case that cubic vertices are present, in the absence of x-type vertices, was already considered in Ref. [19]. Vacant bonds were included as well in that work. The coding used there was basically the coding for random-cluster connectivities [40], which is sufficient because the completely packed cubic connectivities are a subset of the set of random-cluster connectivities. However, for larger system sizes it is only a relatively small subset, which leads to a reduction of the efficiency of the algorithm and of the largest possible system size. For this reason we constructed a coding algorithm for the completely packed cubic connectivities without the use of the random-cluster algorithm.

The principle is summarized as follows. Represent the configuration of dangling bonds by a row of L integers, such that equal integers describe connected bonds and that unequal integers describe unconnected bonds. We refer to this L-site cubic connectivity as the level-zero connectivity. On the basis of these L integers one may perform the following steps:

(i) Let the size of the cluster containing site 1 (the number of connected dangling bonds that include dangling bond 1) be n_1. This cluster can be characterized by a bit string of L bits containing n_1 ones. However, not all such bit strings are allowed. The first bit is always 1 and may be skipped, and since the number of zeros interlaced between a pair of consecutive ones can only be even, one may also skip one half of the zeros. The cluster containing site 1 is thus characterized by means of a unique bit string of length $(L + n_1)/2 - 1$ with an odd number of ones. These bit strings are simply coded and decoded in lexicographic order by using the binomial distribution.

(ii) Let the zeros in the bit string occur in n_g groups separated by one or more ones. As a consequence of the well-nestedness property, the sites in each of these groups cannot be connected to sites in other groups. These groups, called "level-1 connectivities," are still represented by rows of integers, which, for a given site, keeps the same value as for the original level-0 connectivity. The degrees of freedom of the level-0 connectivity that are not accounted for by the enumeration of the level-0 bit string are thus represented by n_g connectivities on less than L points. The coding of the original cubic connectivity is completely specified by the level-0 bit string code, supplemented with the n_g level-1 connectivities.

(iii) One can now analogously perform the operations specified in steps (i) and (iii) for each of the n_g level-1 connectivities. This will yield the enumeration of the level-1 bit strings, and may also lead to a number of level-2 connectivities, and so on. The process ends at the level that yields 0 subgroups for the next level.

This process generates a treelike structure of which the relevant data, i.e., the bit string codes, the number of subgroups, their length, and the position of the first site of that subgroup, are stored for all subsequent levels. After completion of the tree, this information can be transformed into a unique number: the code the L-point connectivity. For that purpose one has to define an ordering of the connectivities, which can, on level 0, be done using the number of sites connected to site 1, combined with the code of the bit string describing the cluster containing site 1. The same type of ordering is applied to subrows at all levels. Those at the highest level are assigned the number 1, and the ordering then determines the enumeration at the next-highest level, and so on until level 0.

d. $z \neq 0, x \neq 0, c \neq 0$

In the general case that all three vertex types are simultaneously present, the number of possible connectivities for a given system size becomes even larger, but the coding algorithm actually becomes much simpler. If site 1 belongs to a cluster of n_1 connected sites, the cluster is represented by a bit string of length $L - 1$ with $n_1 - 1$ ones, which may sit on arbitrary positions. This bit string is enumerated according to lexicographic ordering, and the coding assigns a number equal to the connectivity equal to the number of connectivities with a smaller bit string number, plus the number associated with the coding of the remaining $L - n_1$-point connectivity. The latter problem is entirely similar to the original problem and can thus, step by step, be further reduced, until all sites of the remaining connectivity belong to one connected cluster. In that case we assign the number 1 to the remaining connectivity.

e. Odd system sizes

For L-point connectivities with odd L we allow one odd group of dangling bonds, containing one bond for $c = 0$, and an arbitrary odd number of bonds for $c \neq 0$. Coding of these odd connectivities is done by similar methods.

The largest transfer-matrix sizes used for the various types of coding methods are listed in Table VIII.

TABLE VIII. The largest system sizes and the corresponding numbers of connectivities (maximum linear size of the transfer matrix) used in the present calculations for several combinations of the allowed vertex types listed in the first column.

Vertex types	Even/odd	$L_{\max}$	$C_{L_{\max}}$
z	Even	30	9694845
	Odd	27	20058300
z,c	Even	22	8414640
	Odd	19	6906900
z,x	Even	16	2027025
	Odd	15	2027025
z,c,x	Even	14	4373461
	Odd	13	4373461

[1] H. E. Stanley, Phys. Rev. Lett. **20**, 589 (1968).
[2] E. Domany, D. Mukamel, B. Nienhuis, and A. Schwimmer, Nucl. Phys. B **190**, 279 (1981).
[3] B. Nienhuis, Phys. Rev. Lett. **49**, 1062 (1982); J. Stat. Phys. **34**, 731 (1984).
[4] H. W. J. Blöte and B. Nienhuis, J. Phys. A **22**, 1415 (1989).
[5] B. Nienhuis, Int. J. Mod. Phys. B **4**, 929 (1990).
[6] Y. M. M. Knops, B. Nienhuis, and H. W. J. Blöte, J. Phys. A **31**, 2941 (1998).
[7] Q. Liu, Y. Deng, T. M. Garoni, and H. W. J. Blöte, Nucl. Phys. B **859**, 107 (2012).
[8] H. W. J. Blöte and M. P. Nightingale, Phys. A (Amsterdam) **129**, 1 (1984).
[9] M. J. Martins, B. Nienhuis, and R. Rietman, Phys. Rev. Lett. **81**, 504 (1998).
[10] B. Nienhuis, in *Phase Transitions and Critical Phenomena*, edited by C. Domb and J. L. Lebowitz (Academic Press, London, 1987), Vol. 11.
[11] W.-A. Guo and H. W. J. Blöte, Phys. Rev. E **83**, 021115 (2011).
[12] H. W. J. Blöte and B. Nienhuis, Phys. Rev. Lett. **72**, 1372 (1994).
[13] M. T. Batchelor, H. W. J. Blöte, B. Nienhuis, and C. M. Yung, J. Phys. A **29**, L399 (1996).
[14] C. L. Schultz, Phys. Rev. Lett. **46**, 629 (1981).
[15] J. H. H. Perk and C. L. Schultz, in *Proceedings of the RIMS Symposium on Non-Linear Integrable Systems*, edited by M. Jimbo and T. Miwa (World Scientific, Singapore, 1983), p. 135; in *Yang-Baxter Equation in Integrable Systems*, edited by M. Jimbo (World Scientific, Singapore, 1990), p. 326; J. H. H. Perk (private communication).
[16] O. Babelon, H. J. de Vega, and C.-M. Viallet, Nucl. Phys. B **200**, 266 (1982).
[17] H. J. de Vega and E. Lopes, Phys. Rev. Lett. **67**, 489 (1991).
[18] V. A. Fateev, Yad. Fiz. **33**, 1419 (1981) [Sov. J. Nucl. Phys. **33**, 761 (1981)].
[19] W.-A. Guo, X.-F. Qian, H. W. J. Blöte, and F. Y. Wu, Phys. Rev. E **73**, 026104 (2006).
[20] J. H. H. Perk and F. Y. Wu, Phys. A (Amsterdam) **138**, 100 (1986).
[21] This equivalence was suggested in a referee report for Ref. [11]. We thank the referee for this valuable suggestion.
[22] J. L. Cardy, in *Phase Transitions and Critical Phenomena*, edited by C. Domb and J. L. Lebowitz (Academic Press, London, 1987), Vol. 11.
[23] R. J. Baxter, S. B. Kelland, and F. Y. Wu, J. Phys. A **9**, 397 (1976).
[24] E. H. Lieb, Phys. Rev. Lett. **18**, 1046 (1967).
[25] R. J. Baxter, J. Phys. C **6**, L445 (1973).
[26] H. W. J. Blöte, Y. Wang, and W.-A. Guo, J. Phys. A **45**, 494016 (2012).
[27] E. H. Lieb and F. Y. Wu, in *Phase Transitions and Critical Phenomena*, edited by C. Domb and M. S. Green (Academic Press, London, 1972), Vol. 1.
[28] R. J. Baxter, *Exactly Solved Models in Statistical Mechanics* (Academic Press, London, 1982).
[29] R. Rietman, Yang-Baxter Equations, Hyperlattices and a Loop Model, Ph.D. thesis, University of Amsterdam, 1993.
[30] M. T. Batchelor and H. W. J. Blöte, Phys. Rev. Lett. **61**, 138 (1988); Phys. Rev. B **39**, 2391 (1989).
[31] M. T. Batchelor, B. Nienhuis, and S. O. Warnaar, Phys. Rev. Lett. **62**, 2425 (1989).
[32] S. O. Warnaar, M. T. Batchelor, and B. Nienhuis, J. Phys. A **25**, 3077 (1992).
[33] M. P. M. den Nijs, J. Phys. A **17**, L295 (1984).
[34] H. W. J. Blöte, J. L. Cardy, and M. P. Nightingale, Phys. Rev. Lett. **56**, 742 (1986).
[35] M. J. Martins and B. Nienhuis, J. Phys. A **31**, L723 (1998).
[36] J. de Gier and B. Nienhuis, J. Stat. Mech. (2005) P01006.
[37] J. L. Jacobsen, N. Read, and H. Saleur, Phys. Rev. Lett. **90**, 090601 (2003).
[38] A. Nahum, P. Serna, A. M. Somoza, and M. Ortuño, Phys. Rev. B **87**, 184204 (2013).
[39] I. Guim, H. W. J. Blöte, and T. W. Burkhardt, J. Phys. A **30**, 413 (1997).
[40] H. W. J. Blöte and M. P. Nightingale, Phys. A (Amsterdam) **112**, 405 (1982).
[41] I. Affleck, Phys. Rev. Lett. **56**, 746 (1986).
[42] J. L. Cardy, J. Phys. A **17**, L385 (1984).
[43] Z. Fu, W.-A. Guo, and H. W. J. Blöte, Phys. Rev. E **87**, 052118 (2013).